rates as a function of temperature and aqueous fluid composition

B.Y. Zhen-Wu[1,2*]; K. Dideriksen[2]; J. Olsson[2]; P.J. Raahauge[1]; S.L.S. Stipp[2]; E.H. Oelkers[3,4*]

[1] Maersk Oil and Gas A/S, Esplanaden 50, 1263 Copenhagen K, Denmark

[2] Nano-Science Center, Department of Chemistry, University of Copenhagen, Universitetsparken 5, 2100 Copenhagen Ø, Denmark

[3]GET, CNRS/UMR 5563-OMP-Université de Toulouse, 14 Avenue Edouard Belin, 31400 Toulouse, France

[4] Earth Sciences, University College London, Gower Street WC1E 6BT London, United Kingdom

[*]e-mails: biyun.zhen@maerskoil.com, oelkers@get.obs-mip.fr

Abstract

Barite dissolution and precipitation rates were investigated in closed system reactors, in which total aqueous NaCl concentrations ranged from 0 to 1.5 molal, pH from 2 to 9, and temperature from 25 to 90 °C. Measured barite dissolution and precipitation rates exhibited a reaction order of 0.2 and 1, respectively, with respect to the barite saturation state. Although these different reaction orders suggest distinctly different mechanisms for dissolution and precipitation, the rates for both processes approach equilibrium with a similar slope on a rate versus saturation state plot, consistent with the concept of micro-reversibility. Barite dissolution rate constants increase as a linear function of the square root of ionic strength but vary only slightly with pH. The dissolution rate dependence on temperature is consistent with an activation energy of 25 ± 2 kJ mol^{-1}. Barite dissolution and precipitation rates are not significantly affected by the presence of aqueous calcium, magnesium or strontium. The rates measured in the study were generated in fluids similar to those found in sedimentary basins, ocean floor sediments and oil field reservoirs so the data may provide close estimates for the reactivity of barite during a variety of natural and industrial processes.

Keywords: $BaSO_4$, dissolution, precipitation, kinetics, ionic strength, pH, calcium, magnesium, strontium, mixing ratios.

1. Introduction

This study focuses on the dissolution and precipitation kinetics of barite ($BaSO_4$) for a number of reasons. First, barite formation provides insight into the composition and behaviour of past and present oceans. For example, the isotopic and elemental compositions of barite is used to trace past seawater chemistry, can aid in the understanding of fluid flow and sedimentary redox processes, and provide insight into past ocean productivity (Paytan and Griffith, 2007; Paytan *et al.*, 2007; Griffith and Paytan, 2012). Although seawater is generally undersaturated with respect to barite, it is commonly found in the water column and in marine sediments (Chow and Goldberg, 1960; Wolgemuth and Broecker, 1970; Church and Wolgemuth, 1972; Chan *et al.*, 1977; Falkner *et al.*, 1993). Second, barite is a common precipitate in oil reservoirs and pipelines, where it can impede fluid flow (Vetter *et al.*, 1982; Bezerra *et al.*, 1990; Sorbie and Mackay, 2000; Mackay *et al.*, 2003). It is anticipated additional data on barite dissolution and growth rates could provide insight into how to avoid such clogging. Third, barite readily dissolves and precipitates at ambient conditions (Christy and Putnis, 1993; Dove and Czank, 1995). As such, it is possible to determine barite dissolution and precipitation rates at near to identical conditions to elucidate the degree to which these two processes are linked, and if it may be possible to estimate precipitation from dissolution rates. To improve our understanding of barite reactivity at ambient conditions, we have measured its dissolution and precipitation rates in batch reactor systems. The purpose of this paper is to report these results so they can be applied to elucidate barite reactivity in natural and industrial processes.

A number of studies have explored the rates and mechanisms of barite-water interaction (Collins and Leineweber 1956; Walton, 1963; Klein and Fontal, 1964; Mealor and Townshend, 1966; Gunn and Murthy, 1972; Symeopoulos and Koutsoukos, 1992; Murthy, 1994; Pina *et al.*, 1998) and others have derived the reaction order of barite-fluid reactions using conductivity techniques (Nielsen, 1958; 1959; Nancollas, 1968; Nancollas and Purdie, 1963; Nancollas and Liu, 1975; Liu *et al.*, 1976; Rizkalla, 1983; Cheng *et al.*, 1984; Nielsen and Toft, 1984; Wat *et al.*, 1992; van der Leeden *et al.*, 1992; Taguchi *et al.*, 1996) or activity methods (Bovington and Jones, 1970). Studies of barite dissolution and precipitation mechanisms have also been used to provide insight into polypitting and aggregation (Dunn *et al.*, 1999; Tang *et al.*, 2001; Judat and Kind, 2004; Kuwahara, 2011; Jones, 2012).

Bulk barite dissolution and precipitation rates in NaCl-bearing aqueous solutions have been reported by Christy and Putnis (1993) and Dove and Czank (1995). Christy and Putnis (1993) suggested that barite dissolves via a first order reaction with respect to its saturation state and reported that there was no effect of dissolved NaCl, on the rate at concentrations up to at least 0.1 molar. In addition, they concluded that barite precipitation rates increase with a second order dependence with respect to barium concentration but is pH independent. Dissolution and growth rates for barite have been extrapolated from atomic force microscopic (AFM) measurements by Higgins *et al.* (1998) and Godinho and Stack (2015). Other AFM studies demonstrated that factors including ionic strength and degree of reactive fluid supersaturation influence barite nucleation and crystal morphology (Bosbach *et al.*, 1998; Risthaus *et al.*, 2001; Kowacz and Putnis, 2008; Kowacz *et al.*, 2010). Note, however, that AFM studies tend to generate reaction rates on a single barite surface, whereas bulk rate experiments generate a surface area averaged reaction rates for all of the barite surfaces exposed to the aqueous fluid. As such, AFM rates may not be directly comparable to corresponding bulk rates. Other studies have explored the effect of the aqueous barium to sulfate ratio and the presence of other dissolved ions on barite morphology, surface energy and reaction kinetics (Walton and Walden, 1946; Buchanan and Heymann, 1949; Benton *et al.*, 1993; Wong *et al.*, 2001; Marchisio *et al.*, 2002; Kucher *et al.*, 2006; Kowacz *et al.*, 2007; Steyer and Sundmacher, 2009). Granbakken *et al.* (1991) modeled barite dissolution and precipitation with data taken from the literature. This study builds upon these past efforts by measuring barite dissolution and precipitation rates as a function of ionic strength, pH, total mineral surface area, presence of the divalent cations such as calcium (Ca), magnesium (Mg) and strontium (Sr), the presence of barite seeds, and the initial reactive fluid Ba to SO_4 mole ratio. All experiments were performed in closed system reactor at 25, 60, and 90 °C.

2. Background

The standard state adopted in this study is one of unit activity for pure minerals and water at any temperature and pressure. The standard state for aqueous species is taken as unit activity for the solute in a hypothetical one molal solution extrapolated to infinite dilution. Barite dissolution and precipitation can be described using:

$$BaSO_{4(barite)} = Ba^{2+}_{(aq)} + SO_4^{2-}{}_{(aq)}. \quad (1)$$

In accord with the standard state, the saturation state of the fluid with respect to barite (can be determined using:

, (2)

where corresponds to the activity of the subscripted aqueous species and refers to the equilibrium constant for Reaction 1. Thermodynamic constants and activity coefficients required to determine saturation states with Eqn. 2 were generated using PHREEQC, Version 3 (Parkhurst and Appelo, 2013) together with its Pitzer database (Plummer *et al.*, 1988). The Pitzer approach was adopted in as it more accurately describes barite solubility in the high ionic strength aqueous solutions used in this study.

Dissolution and precipitation rates were obtained from closed system reactors from the slope of reactive fluid concentration versus time plots and normalised to the total mineral surface area in accord with:

, (3)

where stands for the surface area normalised dissolution or precipitation rate, signifies the concentration of th element in the reactive fluid, designates time, corresponds to the total mineral surface area, and represents the mass of fluid in the reactor. Surface-controlled dissolution and precipitation rates are commonly fit to the following empirical rate law:

, (4)

where *k* refers to a rate constant and *n* denotes the reaction order. The form of Eqn. 4 is similar to transition state theory mineral dissolution and precipitation rate equations (Aagaard and Helgeson, 1982; Oelkers, 2001; Oelkers *et al.*, 1994; Schott and Oelkers, 1995; Schott *et al.*, 2009; 2012):

, (5)

where refers to the forward dissolution rate. The parameter *n'* in Eqn. 5 is the product of the Temkin's stoichiometric number and a reaction order that depends on the mechanism; Temkin's stoichiometric number is equal to the ratio of the rate of destruction of the activated or precursor complex relative to the overall rate (Temkin, 1963). A reaction order of 1 is typically attributed to linear growth and a reaction order of 2 to spiral growth.

3. **MATERIALS AND METHODS**

112 The dissolution and precipitation rates of minerals can be influenced by the pretreatment of
113 the solids (Bosbach, 2002; Lasaga and Lüttge, 2004; Schott *et al.*, 2012; Fischer *et al.*, 2012; 2014).
114 In an attempt to limit such effects, a minimal preparation of the starting barite was performed.
115 Natural barite was crushed, sieved, washed with ultrapure deionised (18 mΩ MilliQ) water while
116 shaking to both remove adhering particles and to equilibrate the crushed grain surfaces with the
117 aqueous fluid, then dried at 120 °C. X-ray diffraction (XRD) patterns of these solids showed that
118 samples consisted of barite and contained no other crystalline phases within the detections limits of
119 the XRD which are estimated to be ±3 volume percent. Grains of 1.25-1.5 mm diameter were
120 selected for the experiments. The specific surface area was measured with a Quantachrome
121 Instruments Autosorb-1 using the BET method, with krypton as the adsorbate gas. The surface area
122 was 0.006 $m^2\ g^{-1}$ (± 10%). The geometric surface area, calculated assuming cube shaped grains,
123 with an average diameter of 1.38 mm and density of 4.48 g cm^{-3}, was 0.001 $m^2\ g^{-1}$. These solids
124 were further analysed both before and after selected experiments by scanning electron microscopy
125 (SEM), using a FEI Quanta 3D SEM and by X-ray photoelectron spectroscopy (XPS), using a
126 Kratos Axis Ultra XPS.

127 Closed system experiments at 25 and 60 °C were performed in acid-washed polypropylene
128 Nalgene© reaction vessels, placed in a THERMOLAB GFL 1083 temperature-controlled,
129 reciprocating motion shaking bath that is similar to the reactor systems used by Harouiya *et al.*
130 (2007). Initial reactive fluids were prepared by adding selected quantities of analytical grade (≥99%,
131 Sigma Aldrich) NaCl, Na_2SO_4, $BaCl_2{\cdot}2H_2O$, $CaCl_2{\cdot}2H_2O$, $MgCl_2{\cdot}6H_2O$, and $SrCl_2{\cdot}6H_2O$ to
132 ultrapure water. The composition of all initial fluids is listed in Table 1. Experiments were initiated
133 by first temperature equilibrating the initial fluids, minerals and reactors to 25 or 60 °C.
134 Approximately 200 g of reactive fluid and ~0.5 g of barite were then added to the reactors, which
135 were then sealed. Each experiment ran for seven to ten days so that fluid-barite equilibrium could
136 be attained (see below). Reactor fluid samples were collected using syringes fitted with 0.45 μm
137 cellulose acetate membrane filters. Each fluid sample was immediately weighted and divided. One
138 fraction of this fluid was diluted with 2% HNO_3 for inductively coupled plasma atomic emission
139 spectroscopy (ICP-AES) analysis. Another fraction of the sample was used for pH measurement,
140 with a combined pH electrode coupled to a Metrohm 713 pH meter. Prior to its use, the electrode
141 was calibrated with NBS traceable pH 4.002, 6.881 and 9.224 buffer solutions at 21 °C.
142 Experiments at 90 °C were performed in hydrothermal, closed system, titanium reactors, fitted with

143 a 5 μm filter and designed for 180º rotation for fluid/mineral mixing at liquid-vapor saturation
144 pressure.

145 Analysis of aqueous concentrations of barium, sulfur, calcium, magnesium and strontium
146 were performed using a Horiba Jobin Yvon, Ultima 2 ICP-AES, with detection and quantification
147 limits of: 9×10^{-10} mol kg^{-1} and 3×10^{-9} mol kg^{-1} for Ba; 4×10^{-7} mol kg^{-1} and 1×10^{-6} mol kg^{-1} for
148 S; 1×10^{-6} mol kg^{-1} and 3×10^{-6} mol kg^{-1} for Ca; 1×10^{-9} mol kg^{-1} and 3×10^{-10} mol kg^{-1} for Sr. The
149 standard deviation of the analytical results is less than 5%. To minimize matrix effects during
150 analysis, all standards were prepared with the same matrix as the diluted fluid samples. All the
151 initial reactive fluids, dilutions and standards were prepared by weighing.

152 **4. RESULTS**

153 ***4.1 Observations of the solid phase***

154 Representative SEM images of the barite prior to and following the experiments are shown
155 in Fig. 1. Prior to the experiments, the barite crystals had flat surfaces that were free of other
156 mineral phases except a dusting of <500 nm diameter particles that adhered to the larger grain
157 surfaces (Fig. 1a). After dissolution, etch pits had formed (Fig. 1b). Precipitation resulted in the
158 smoothing of seed crystal terraces and the formation of rhomboidal crystals (Fig. 1c). Some
159 examples of the range of barite morphology resulting from dissolution or precipitation in various
160 fluids are shown in Figs. 1d to f. In all cases, dissolution induces etch pit formation and
161 precipitation is dominated by growth on existing seed crystals.

162 ***4.2 Temporal reactive fluid phase evolution during closed system dissolution and precipitation***
163 ***experiments***.

164 The evolution of the fluid composition during all experiments is provided in the electronic
165 supplement. All measured reactive fluid Ba and SO_4 concentrations and pH have been included. The
166 Ba to SO_4 mole ratios for the reactive fluids are consistent with stoichiometric release from
167 dissolving barite or precipitation of stoichiometric barite, with the exception of several
168 measurements at the beginning of the experiments. This initial behavior probably reflects analytical
169 uncertainties in the measurement of small changes in fluid composition.

170 Initial experiments at 25 ^{o}C and 1 molal NaCl were designed to assess the effect of aqueous
171 fluid mixing on measured barite rates. The results of these experiments are presented in Fig. 2a. The

change in barium concentration upon the precipitation and dissolution of barite during experiments performed at shaking speeds of 0.2, 1.3 and 2.8 cycles per second is shown in this figure. The dissolution and precipitation rates obtained from experiments performed at 1.3 cycles s^{-1} are no more than twice the corresponding rates obtained from experiments performed at 0.2 cycles s^{-1}. In contrast, rates obtained from experiments performed at 2.8 cycles s^{-1} are approximately 4 times faster than those obtained from the 1.3 cycles s^{-1} experiments (see below and Tables 1 and 2). Most notably, aqueous barite concentrations in the dissolution experiments performed at 2.8 cycles s^{-1} exceed that of barite-fluid equilibrium, as indicated by the dashed line, after two days of elapsed time before decreasing to a final value less than its equilibrium concentration. Such a behavior can arise due to the abrasion of barite surfaces, which could have resulted from the vigorous stirring of the reactor during these experiments. As such, and to avoid potential ambiguities due to stirring rates, all subsequent experiments reported in this study were performed at the intermediate stirring rate of 1.3 cycles s^{-1}.

Further experiments designed to determine conditions at which barite growth can be studied in the absence of heterogeneous nucleation were performed at 25 ^{o}C and 0.1 molal NaCl. The temporal evolution of Ba concentration during the unseeded experiments, where the Ba:SO_4 was 1:1, and the initial fluid saturation states with respect to barite were 3, 8 and 34, are illustrated in Fig. 2b. The reactive fluid Ba concentration is constant throughout the experiment when the initial fluid saturation state is 3 and 8 in the absence of barite seeds, consistent with no barite precipitation, but fluid Ba concentration decreases in the experiment with an initial fluid saturation state of 34, as expected for nucleation and growth of a Ba phase. In contrast, for the corresponding seeded growth experiments (Fig. 2c), Ba concentration decreases when the initial fluid saturation state is 3, 8 or 34, consistent with barite precipitation. To ensure that rates measured in this study avoided the effects of heterogeneous nucleation, all further barite growth experiments reported in this study were performed with a subsample of the same barite seed crystal stock and all initial reactive fluids had a saturation state with respect to barite of 8 or less.

The change in barium concentration during the closed system dissolution and precipitation experiments at 25 and 60 °C, in aqueous solutions at four different ionic strengths and having a 1:1 molar Ba to SO_4 ratio, is presented in Fig. 3. Barium concentration systematically approaches the same value from both under and oversaturated conditions. In all cases, steady state is reached within ~10 days at 25 °C and within ~6 days at 60 °C. The dashed lines correspond to the presumed

equilibrium barium concentrations in the experiments. The equilibrium Ba concentration at 25 °C increases from 1.2 x 10^{-5} to 8 x 10^{-5} mol kg^{-1} as dissolved NaCl concentration increases from 0 to 1.5 mol kg^{-1}, consistent with the influence of ionic strength on barite solubility. Experiments at 90 °C were only performed from undersaturated solutions (Fig. 4). An ionic strength dependence is nevertheless clear and Ba concentration approaches steady state significantly faster at 90 °C than at ambient temperature.

The temporal variation of reactive fluid Ba concentrations during experiments performed at pH 2, 3, 6.5, 9, and 10 are shown in Fig. 5. The approach to equilibrium is similar for the three experiments in acidic to circumneutral conditions, though with a slight rate increase as pH increases. At basic pH, the approach to equilibrium is slower and the steady state Ba concentration is also lower.

The temporal variations of reactive fluid Ba concentrations during additional experiments are presented in Figs. 6 to 8. Experiments performed in the presence of 0.1, 0.5, and 1.0 g of barite are shown in Fig. 6. The approach of the fluid composition to steady state is similar for the experiments performed with 0.5 and 1.0 g but that performed using 0.1 g is significantly slower. The fluid phase evolution of experiments performed in the presence of aqueous Ca, Mg, and Sr are shown in Fig. 7. The concentrations of divalent metals added to the initial reactive fluids were 10^{-3}, $6x10^{-2}$, and 10^{-5} mol/kg, respectively, for Ca, Mg, and Sr; these concentrations were chosen such that the reactive fluids would be undersaturated with respect to potentially precipitating divalent metal sulfate phases. As was the case for the experiments at various NaCl concentrations shown in Fig. 3, experiments performed at 25 °C and in the presence of aqueous Ca, Mg, and Sr from under- and super-saturated conditions approach the same stationary-state Ba concentrations. Because of the strong effect of aqueous fluid ionic strength on barite solubility, the NaCl-free, Mg and Ba bearing initial fluid used in experiment 1PM was undersaturated with respect to barite. As such, the two experiments performed in aqueous NaCl-free, Mg-bearing initial reactive fluids (Fig. 7c) were both initiated from undersaturated conditions. Fig. 8 shows the change in fluid Ba concentration during barite precipitation as a function of initial fluid $Ba:SO_4$ mole ratios, but with identical initial barite saturation states. The approach to steady state is similar for $Ba:SO_4$ of 1:16 and 1:64, whereas for 1:4, it is slightly faster.

4.3 Derivation of reaction orders and rate constants.

Rate constants and reaction orders are determined by fitting the reactive fluid Ba concentrations, listed in Table 2 and shown in Figs. 3 to 8. The regression was performed by numerical integration of Eqn. 5, using an excel spreadsheet, by the method of Harouiya *et al.* (2007). Eqn. 5 was used for this purpose rather than Eqn. 4, as the former is consistent with transition state theory. The values of the rate constant, , and the reaction order, , were adjusted by trial and error to obtain the closest match between the calculated and measured Ba concentration data. The results for the barite precipitation experiments were consistent with a reaction order of 1 and the rate constants listed in Table 2. The solid curves passing through the reactive fluid concentration data in Figs. 2 to 8 validate these regression calculations. The reaction orders were derived with respect to barite saturation state, rather than with respect to the concentration of either aqueous barium or sulfate. This is an important distinction. A number of past studies interpreted barite precipitation to be a second order reaction with respect to Ba concentration (e.g. Christy and Putnis, 1993). There are two aqueous species in the barite dissolution/precipitation reaction, Ba and SO_4, so a first order reaction with respect to barite saturation state is equivalent to a second order reaction with respect to either aqueous barium or aqueous sulfate concentration, or first order with respect to both aqueous barium and sulfate concentration. Attempts to fit the change in Ba concentration during dissolution experiments with a first order reaction with respect to barite saturation state failed, as shown by Fig. 9. The best fit for all of the dissolution results was obtained for = 0.2, with respect to barite.

5. DISCUSSION

5.1 Variation of barite dissolution and precipitation rates with reactive fluid composition

Barite is known to form in natural fluids at a range of salinities. A number of studies suggest that the logarithm of reaction rates is proportional to the square root of the ionic strength (Perlmutter-Hayman and Persky, 1960; Leininger and Westley, 1968; Wood, 1973; Jacobsen, 1977; Tsukahara, 1986; Matthis and Erman, 1995; Pedersen *et al.*, 1995; García-García *et al.*, 2007). We tested this relationship with the aid of Fig. 10. The rate constants increase by 0.5 to 1 order of magnitude as the NaCl concentration increases from 0 to 1.5 mol kg^{-1} at 25, 60 and 90 °C. The linear regression in Fig. 10 is similar at 60 and 90 °C; the slope of the least-squares fit to the barite dissolution rates is 0.6 for both sets of data. There is more scatter in the data at 25 °C; the reason for this poor consistency is unclear. The results contrast somewhat with those of Christy and Putnis (1993), who concluded that there was little to no effect of aqueous solution ionic strength on barite

dissolution rates up to 0.1 mol L^{-1} NaCl. Nevertheless, Risthaus *et al.* (2001), Kowacz and Putnis (2008) and Kowacz *et al.* (2010) showed, using AFM, that ionic strength influences significantly crystal dissolution and growth rates.

The dissolution rate of many minerals depends strongly on pH (e.g. Marini, 2007; Schott *et al.*, 2009). Its effect on barite dissolution rates in 1 mol kg^{-1} NaCl solution is shown in Fig. 11. At 25 °C, dissolution rates vary only slightly with pH; the logarithm of measured rate constants determined from pH 2 to 10 range from -6.3 < < -6.9. The linear regression of these dissolution rates suggests a slight decrease as pH increases, though the trend is not strong. Our observations are somewhat similar to those of Dove and Czank (1995), who reported that barite dissolution rate constants decrease by ~1.5 orders of magnitude as the pH was increased from 2 to 12. In contrast, Ruiz-Agudo *et al.* (2015) suggested that barite growth rates are enhanced at pH > 10, because of the alteration of the mineral surface caused by the presence of hydroxyl ions.

As the data in Table 2 suggest, the presence of Ca, Mg and Sr has a negligible influence on barite dissolution and precipitation rates at 25 °C. The logarithm of the geometric surface area normalised dissolution rate constant in 1 mol kg^{-1} NaCl solutions, in the absence of added divalent cations is -6.42, comparable to those observed when the divalent ions are present, i.e. for Ca, it is -6.49, for Mg, -6.48 and for Sr, -6.40. Note that the concentration of Ca, Mg, and Sr chosen for these experiments differ; for Ca and Sr, these concentrations were chosen to be no more than 25% of the solubility concentration of the corresponding divalent cation sulfate phases (e.g. gypsum and celestite) in the initial reactive fluid. $MgSO_4$ is very soluble, so the Mg concentration was set to match that of seawater. Magnesium addition significantly increased the ionic strength in the NaCl-free experiments, thus increasing barite solubility. Therefore, the increase in barite dissolution rates in the presence of Mg in the NaCl-free experiments is likely attributable to increased ionic strength rather than an effect of the Mg ion. This conclusion is supported by the results of experiments performed in the presence of 1 mol kg^{-1} aqueous NaCl, for which the rate was nearly identical to that determined in the corresponding Mg-free experiment. These observations are consistent with those of Gardner and Nancollas (1983), who reported that the barite growth rate at 125 °C and 0.2 mol L^{-1} NaCl is independent of the presence of Sr at concentrations similar to those used in this study. However, Gardner and Nancollas (1983) reported the formation of a $(Ba,Sr)SO_4$ solid solution in the presence of aqueous Sr. Similarly, Benton *et al.* (1993) suggested that, at 95 °C, the presence of Ca would affect barite precipitation rates because of the formation of a $(Ba,Ca)SO_4$

295 solid solution. Likewise, Pina *et al*. (2000) concluded that substantial Sr co-precipitated with barite
296 at 25 °C from NaCl-free Sr-bearing aqueous fluids. We found no evidence of solid solution
297 formation in our experiments. X-ray photoelectron spectroscopy (XPS) of the barite recovered from
298 25 °C experiments showed no sign of Mg, Sr or Ca in the top ~10 nm of the mineral surface, even
299 though XPS is able to identify as little as 1% of a trace element within the top few nanometres of a
300 surface. Furthermore, analyses of the aqueous concentration of Ca, Mg and Sr show no detectable
301 variation. The differences in the observations performed in this study compared to that of Pina *et al*.
302 (2000) are likely attributable to the lower aqueous Sr concentrations used in the present study. The
303 reactive aqueous fluids used in the Pina *et al*. (2000) study contained 2 to 3 orders of magnitude
304 higher Sr concentrations than in the present study, such that celestite solid solutions were
305 substantially supersaturated (c.f. Prieto, 2009).

306 In most natural Earth surface waters, the concentration of dissolved sulfate greatly exceeds
307 that of barium. For example, the $Ba:SO_4$ mole ratio for seawater is 10^{-4} (Hanor, 2000; Li and
308 Schoonmaker, 2003; Holland, 2007; Griffith and Paytan, 2012). Experiments to assess the effect of
309 the relative concentration of aqueous barium versus sulfate were performed in this study by varying
310 the $Ba:SO_4$ ratio of the initial solution at a constant degree of saturation. The resulting rate constants
311 are presented in Table 2. Although the data suggest a slight decrease of barite precipitation rates
312 with increasing sulfate concentration, the effect is minimal. The rate constant in the experiments
313 with an initial 1:64 ratio is less than 0.2 orders of magnitude lower than in a solution where $Ba:SO_4$
314 = 1. This observation contrasts with that of Rizkalla (1983) who suggested that barite precipitation
315 rates are faster when the reactive fluid has a different $Ba:SO_4$ ratio than barite.

316 ***5.2 Correlation of reaction rate with total mineral surface area***

317 It is commonly assumed that mineral dissolution rates are proportional to the surface area of
318 the mineral-fluid interface. This was tested by a set of barite dissolution experiments where the
319 initial barite seed crystal mass was 0.1, 0.5 and 1.0 g in 200 g of solution. The rate constants for
320 these experiments, listed in Table 2 decrease with increasing barite mass, i.e. by ~0.25 log units for
321 mass increase from 0.1 to 1 g. The difference is only marginally significant, quite close to the
322 uncertainty limit. Such differences, however, suggest that the rates are not completely proportional
323 to barite surface area, perhaps due to distinct reactivity of distinct parts of the barite surface. For
324 example, larger grains have fewer edge sites; such sites tend to be more reactive, as evidenced by
325 grain rounding during dissolution (Crook, 1968; Gautier *et al.*, 2001). The consequences of distinct

reaction rates of various mineral surfaces on overall bulk mineral dissolution rates have been explored in detail by Lasaga and Lüttge (2004) and Fischer *et al.* (2012; 2014).

5.3 Dependence of barite dissolution rates with temperature

The dependence of the barite dissolution rate constant as a function of temperature can be described by the Arrhenius equation:

(6)

where represents the Arrhenius pre-exponential factor, denotes an activation energy, represents the gas constant and refers to the absolute temperature. This equation was applied to the data generated in this study using the Arrhenius plots shown in Fig. 12, where the natural logarithm of rate constants for barite dissolution in 0.1, 1.0, and 1.5 mol kg^{-1} NaCl solutions are plotted as a function of the reciprocal absolute temperature. The slope yields an activation energy of 25 ± 2 kJ mol^{-1} and a pre-exponential factor of $(1.6 \pm 1.0) \times 10^{-3}$ mol m^{-2} s^{-1}. This activation energy agrees, within uncertainty, with those reported by Bovington and Jones (1970), Cheng *et al.* (1984), and Christy and Putnis (1993) but is somewhat lower than the value reported by Dove and Czank (1995). This activation energy suggests that barite dissolution was likely to be a surface-controlled reaction, consistent with observations from Christy and Putnis (1993), who reported that their rate constants were independent on the stirring rate. Similar conclusions were reported by Nancollas and Liu (1975) and Liu *et al.* (1976).

Taking account of the observations described above, the dissolution rate constant for barite can be estimated using Eqn. 5 and = 0.2 generated from:

- , (7)

where represents a constant, corresponds to the hydrogen ion activity and denotes the ionic strength of the fluid. Regression of the dissolution rate constants listed in Table 2 to Eqn. (7) yields a best fit of 0.03 for and 0.6 for and of 2.75×10^{-8} mol m^{-2} s^{-1}. This equation together with these parameters reproduces 21 of 27 of the measured rates to within 0.25 log units. Rate constants derived using these parameters are compared to corresponding experimental results in Fig. 13.

5.4 Comparison with past studies

The direct comparison of barite dissolution and precipitation rates determined in this study with those from past work is confounded by several factors. First, previously reported barite rates have been normalised to either geometric or measured BET surface areas. For example, Christy and Putnis (1993) normalised their rates to a calculated geometric surface area, whereas Dove and Czank (1995) normalised their data to measured BET surface area. Second, different studies adopted distinct barite solubility models to interpret their data. Christy and Putnis (1993) and Dove and Czank (1995) used barite solubility constants reported by Blount (1977), which are based on the extended Debye-Hückel equation. These solubility constants differ by as much as 14% from those derived using the Pitzer approach adopted for this study. Note that as barite dissolves and precipitates rapidly, reactive fluids in these barite-water experiments are commonly close to equilibrium conditions, where fluid saturation states, and thus the choice of solubility model influences reaction rates significantly. Third, rates were interpreted using distinct reaction orders. Fourth, our study shows that barite dissolution and precipitation rates depend somewhat on pH but solution pH is not reported in many of the previously published studies.

Considering these factors, it is not surprising that there is considerable variation among the dissolution and precipitation rates reported in the literature. Nevertheless, Godinho and Stack (2015) extrapolated barite growth rates from atomic force microscopy measurements at 22.2 °C and obtained rates that are within one order of magnitude of our experimental results. Dove and Czank (1995) reported that the dissolution rate constant, normalised to BET surface area, from experiments made at 50 °C changed from $10^{-6.8}$ to $10^{-8.1}$ mol m^{-2} s^{-1} as pH increased from 2 to 12. These results are comparable to our BET rate constant of $10^{-7.3}$ mol m^{-2} s^{-1} at 60 °C and a pH of 4.6. Similarly, Higgins *et al.* (1998) extrapolated barite dissolution rates from AFM measurements at 90 °C in NaCl-free fluids. Their rate constant of $10^{-6.96}$ mol m^{-2} s^{-1} is reasonably close to our $10^{-6.3}$ mol m^{-2} s^{-1}, obtained at 90 °C in 0.1 mol kg^{-1} NaCl solutions.

5.5 Consistency between dissolution and precipitation rates

Our experiments were designed in part to elucidate if a link exists between barite dissolution and precipitation kinetics. Transition state theory, the most commonly used formalism for describing the variation of mineral dissolution rates as a function of saturation state, is based on the assumption of the principle of detailed balancing and micro-reversibility of the overall reaction. The principle of detailed balancing is the concept that the forward rate of a process at equilibrium occurs at an equal but opposite rate as the reverse process (Aagaard and Helgeson, 1982; Oelkers, 2001;

Schott *et al.*, 2009; Schott *et al.*, 2012). Numerous minerals, however, do not precipitate at ambient temperature and others cannot grow at low degrees of supersaturation (Pina *et al.*, 1998; Saldi *et al.*, 2009; 2012; Schott *et al.*, 2012). Quantifying the degree to which precipitation rates are related to dissolution rates is essential for predicting the fate and consequences of chemical reactive transport in natural and anthropogenically influenced systems such as those relevant for nuclear waste storage (e.g. Verma and Pruess, 1988; Pruess *et al.*, 2002), geological carbon storage (e.g. Oelkers and Schott, 2005; Xu *et al.*, 2005, Pham *et al.*, 2011; Aradottir *et al.*, 2012; Hellevang *et al.*, 2013; Zhang *et al.*, 2015) and a host of industrial applications, including scaling.

Fitting of the barite dissolution and precipitation rates measured in this study indicate that the reaction orders for the two reactions differ. The data suggest that barite dissolution follows a reaction order of 0.2 but a precipitation reaction order of 1. Nevertheless, as can be seen in Fig. 14, barite dissolution and precipitation rates determined at close to equilibrium conditions at 25 °C converge to an identical slope on the rate versus saturation state plot as they approach equilibrium. Figs. A and B in the electronic supplement show the corresponding plots for barite dissolution and precipitation at 60 °C and in the presence of Ca, Mg, and Sr. These plots were generated using Eqn. 5 and the parameters listed in Table 2 and the fits match strongly to the data shown in Figs. 3 and 8. The fact that the slope of the curves in Figs. 14, A and B do not change as the curves cross equilibrium, lends support to the concept of detailed balancing in spite of the fact that the change in reaction order suggests a change in mechanism as the system moves from undersaturated to supersaturated conditions. A similar confirmation of the concept of detailed balancing was reported from AFM observations on the anhydrite surfaces by Shindo *et al*. (1992) and Pina (2009).

5.6 Implications for natural systems

These results demonstrate that barite rapidly dissolves and precipitates at ambient temperature and the rates increase at 60 and 90 ºC. Dissolution and precipitation rates are not substantially altered by the presence of aqueous Ca, Mg, or Sr. Thus, it is reasonable to assume that barite reactivity is similarly rapid in natural systems. One might expect, therefore, that natural fluids would be locally saturated with respect to barite when the solid is in excess and that barite would rapidly dissolve in undersaturated, natural waters. As the measured barite reaction rates are rapid, the hydrodynamics and chemical transport in the fluid phase need to be taken into account when applying rates of this study to natural systems. An example of the limitation of barite reactivity by chemical transport is likely the observation that barite is common in marine sediments even though

seawater is generally undersaturated with respect to barite (Chow and Golberg, 1960); relatively sluggish chemical transport can lead to local variations in the fluid phase barite saturation states. The concentration of Ba in seawater is also observed to increase with depth because of the decomposition of barium-bearing organic matter settling to the seafloor (Wolgemuth and Broecker, 1970; Ganeshram *et al.*, 2003). This association led González-Muñoz *et al.* (2003; 2012) to speculate that barite precipitation in marine environments is indirectly induced by bacteria.

6. Conclusions

The results of this study illustrate the rates at which barite is likely to dissolve and precipitate in a variety of natural and industrial systems. The rates demonstrate that barite readily achieves equilibrium with its adjacent fluid phase from both undersaturated and supersaturated conditions, over a range of ionic strengths and in the presence of divalent metal cations (Ca, Mg and Sr), at temperatures ranging from 25 to 90 °C. Thus, it can be anticipated that aqueous solution-barite equilibrium is broadly achieved in nature.

A notable observation is that despite the fact that barite dissolution and precipitation appear to proceed via distinct reaction orders, suggesting distinct reaction mechanisms, these rates vary as equal but opposite functions of fluid saturation state at near to equilibrium conditions. This observation seems to confirm the principle of detailed balancing and the concept that barite-fluid equilibrium is a dynamic process. This observation may serve as a guide to extrapolate the dissolution and precipitation rates of other minerals to the near-to-equilibrium conditions typical of numerous natural systems.

Acknowledgements: We are grateful for the technical assistance and helpful discussions provided by Martin Voigt, Philippe Besson, Alain Castillo, Giuseppe Saldi, Thomas Rinder, Ulf-Niklas Berninger, Thierry Aigouy, Jacques Schott, Juan Diego Rodríguez Blanco, Denis Okhrimenko and Nicolas Bovet. We thank the Géosciences Environnement Toulouse (GET) for collaboration and the NanoGeoScience Section for support and encouragement, and to three reviewers for their valuable comments that improved this paper. This work was funded by the European Commission (EC) 7th Framework Marie Curie (MC) Initial Training Network (ITN) grant MINSC (Mineral Scale Formation; #290040). We thank Maersk Oil and Gas A/S and the DUC Partners (Danish

Underground Consortium: A.P. Møller-Mærsk A/S, Shell, Chevron and the Danish North Sea Fund) for permission to publish this paper.

REFERENCES

Aagaard, P. and Helgeson, H. C. (1982) Thermodynamic and kinetic constraints on reaction rates among minerals and aqueous solutions; I, Theoretical considerations. *Amer. J. Sci.* **282**, 237-285.

Aradottir, E. S. P., Sonnenthal, E. L., Bjornsson, G., Jonsson, H. (2012) Multidimensional reactive transport modeling of CO_2 mineral sequestration in basalts at the Hellisheidi geothermal field Iceland. *Int. J. Greenhouse Gas Cont*. **9,** 24-40.

Benton, W. J., Collins, I. R., Grimsey, I. M., Parkinson, G. M. and Rodger, S. A. (1993) Nucleation, growth and inhibition of barium sulfate-controlled modification with organic and inorganic additives. *Faraday Discuss.* **95**, 281-297.

Bezerra, M. C. M., Khalil, C. N. and Rosário, F. F. (1990) Barium and strontium sulfate scale formation due to incompatible water in the Namorado field, Campos Basin, Brazil. *Soc. Petrol. Eng. Latin Amer. Petrol. Eng. Conference* **SPE 21109**, 1-5.

Blount, C. W. (1977) Barite solubilities and thermodynamic quantities up to 300 °C and 1400 bars. *Amer. Mineral.* **62**, 942-957.

Bosbach, D. (2002) Linking molecular-scale barite precipitation mechanisms with macroscopic crystal growth rates. In: *Water-Rock Interactions, Ore Deposits, and Environmental Geochemistry: A tribute to David A. Crerar.* (R. Hellmann and S. A. Wood, eds.). The Geochemical Society **7**, 97-110.

Bosbach, D., Hall, C. and Putnis, A. (1998) Mineral precipitation and dissolution in aqueous solution: in-situ microscopic observations on barite (001) with atomic force microscopy. *Chem. Geo.* **151**, 143-160.

Bovington, C. H. and Jones, A. L. (1970) Tracer study of the kinetics of dissolution of barium sulphate. *Trans. Faraday Soc.* **66**, 764-768.

Buchanan, A. S. and Heymann, E. (1949) The electrokinetic potential of sparingly soluble sulfates. I. *J. Colloid Sci.* **4**, 137-150.

Chan, L. H., Drummond, D., Edmond, J.M. and Grant, B. (1977) On the barium data from the Atlantic GEOSECS expedition. *Deep-Sea Res.* **24**, 613-649.

Cheng, V. K., Coller, B. A. W. and Powell, J. L. (1984) Kinetics and simulation of dissolution of barium sulphate. *Faraday Discuss. Chem. Soc.* **77**, 243-256.

Chow, T. J. and Goldberg, E. D. (1960) On the marine geochemistry of barium. *Geochim. Cosmochim. Acta* **20**, 192-198.

Christy, A. G. and Putnis, A. (1993) The kinetics of barite dissolution and precipitation in water and sodium chloride brines at 44-85°C. *Geochim. Cosmochim. Acta* **57**, 2161-2168.

Church, T. M. and Wolgemuth, K. (1972) Marine barite saturation. *Earth Planet. Sci. Lett.* **15**, 35-44.

Collins, F. C. and Leineweber, J. P. (1956) The kinetics of the homogeneous precipitation of barium sulfate. *J. Phys. Chem.* **60**, 389-394.

Crook, K. A. W. (1968) Weathering and roundness of quartz sand grains. *Sedimentology*, **11**, 171-182.

Dove, P. M. and Czank, C. A. (1995) Crystal chemical controls on the dissolution kinetics of the isostructural sulfates: celestite, anglesite, and barite. *Geochim. Cosmochim. Acta* **59**, 1907-1915.

Dunn, K., Daniel, E., Shuler, P.J., Chen, H. J., Tang, Y. and Yen, T. F. (1999) Mechanisms of surface precipitation and dissolution of barite: a morphology approach. *J. Colloid Interface Sci.* **214**, 427-437.

Falkner, K. K., Klinkhammer, G. P., Bowers, T. S., Todd, J. F., Lewis, B. L., Landing, W. M. and Edmond, J. M. (1993) The behavior of barium in anoxic marine waters. *Geochim. Cosmochim. Acta* **57**, 537-554.

Fischer, C., Arvidson, R. S., Lüttge, A. (2012) How predictable are dissolution rates of crystalline material? *Geochim. Cosmochim. Acta* **98**, 177-185.

Fischer, C., Kurganskaya, I., Schäfer, T., Lüttge, A. (2014) Variability of crystal surface reactivity: What do we know? *Appl. Geochem.* **43**, 132-157.

Ganeshram, R. S., Francois, R., Commeau, J. and Brown-Leger, S. L. (2003) An experimental investigation of barite formation in seawater. *Geochim. Cosmochim. Acta* **67**, 2599-2605.

García-García, S., Wold, S. and Jonsson, M. (2007). Kinetic determination of critical coagulation concentrations for sodium-and calcium-montmorillonite colloids in NaCl and $CaCl_2$ aqueous solutions. *J. Colloid Interface Sci.* **315**, 512-519.

Gardner, G. L. and Nancollas, G. H. (1983) Crystal growth in aqueous solution at elevated temperatures. Barium sulfate growth kinetics. *J. Phys. Chem.* **87**, 4699-4703.

Gautier, J. M., Oelkers, E. H., Schott. J. (2001) Are quartz dissolution rates proportional to BET surface areas? *Geochim. Cosmochim. Acta.* **65,** 1059-1070.

Godinho, J. R. A. and Stack, A. G. (2015) Growth kinetics and morphology of barite crystals derived from face-specific growth rates. *Crystal Growth Des.* **15**, 2064-2071.

González-Muñoz, M. T., Fernández-Luque, B., Martínez-Ruiz, F., Chekroun, K. B., Arias, J. M., Rodríguez-Gallego, M., Martínez-Cañamero, M., de Linares, C. and Paytan, A. (2003) Precipitation of barite by Myxococcus xanthus: possible implications for the biogeochemical cycle of barium. *Appl. Environ. Microb.* **69**, 5722-5725.

González-Muñoz, M. T., Martínez-Ruiz, F., Morcillo, F., Martín-Ramos, J. D. and Paytan, A. (2012) Precipitation of barite by marine bacteria: a possible mechanism for marine barite formation. *Geology* **40**, 675-678.

Granbakken, D., Haarberg, T., Rolheim, M., Østvold, T., Read, P. and Schmidt, T. (1991) Scale formation in reservoir and production equipment during oil recovery. III. A kinetic model for the precipitation/dissolution reactions. *Acta Chem. Scand.* **45**, 892-901.

Griffith, E. M. and Paytan, A. (2012) Barite in the ocean-occurrence, geochemistry and palaeoceanographic applications. *Sedimentology* **59**, 1817-1835.

Gunn, D. J. and Murthy, M. S. (1972) Kinetics and mechanisms of precipitations. *Chem. Eng. Sci.* **27**, 1293-1313.

Harouiya, N., Chairat, C., Kohler, S. J., Gout, R. and Oelkers E. H. (2007) The dissolution kinetics and apparent solubility in closed reactors at temperatures from 5 to 50 C and pH from 1 to 6. *Chem. Geo.* **244,** 554-568.

Hanor, J. S. (2000) Barite–celestine geochemistry and environments of formation. *Rev. Mineral. Geochem.* **40**, 193-275.

527 Helgeson, H. C., Murphy, W. M. and Aagaard, P. (1984) Thermodynamic and kinetic constraints on
528 reaction rates among minerals and aqueous solutions. II. Rate constants, effective surface
529 area, and the hydrolysis of feldspar. *Geochim. Cosmochim. Acta* **48**, 2405-2432.

530 Hellevang H., Pham, V. T. H., Aagaard, P. (2013) Kinetic modeling of CO_2-water-rock interaction.
531 *Int. J. Greenhouse, Gas Contr.,* **15,** 3-15.

532 Higgins, S. R., Jordan, G., Eggleston, C. M. and Knauss, K. G. (1998) Dissolution kinetics of the
533 barium sulfate (001) surface by hydrothermal atomic force microscopy. *Langmuir*, **14**, 4967-
534 4971.

535 Holland, H. D. (2007) The geologic history of seawater. In: *Treatise on Geochemistry, Vol. 6: The*
536 *Oceans and Marine Geochemistry*, 1-46.

537 Jacobsen, J. (1977) Studies of the affinity of human serum albumin for binding of bilirubin at
538 different temperatures and ionic strength. *Int. J. Pept. Protein Res.* ***9***(3), 235-239.

539 Jones, F. (2012) Infrared investigation of barite and gypsum crystallization: evidence from an
540 amorphous to crystalline transition. *Crystal Eng. Commun.* **14**, 8374-8381.

541 Judat, B. and Kind, M. (2004) Morphology and internal structure of barium sulfate-derivation of a
542 new growth mechanism. *J. Colloid Interface Sci.* **269**, 341-353.

543 Klein, D. H. and Fontal, B. (1964) Heterogeneous and homogeneous nucleation of barium sulphate.
544 *Talanta* **11**, 1231-1237.

545 Kowacz, M. and Putnis, A. (2008) The effect of specific background electrolytes on water structure
546 and solute hydration: consequences for crystal dissolution and growth. *Geochim. Cosmochim.*
547 *Acta* **72**, 4476-4487.

548 Kowacz, M., Prieto, M. and Putnis, A. (2010) Kinetics of crystal nucleation in ionic solutions:
549 Electrostatics and hydration forces. *Geochim. Cosmochim. Acta* **74**, 469-481.

550 Kowacz, M., Putnis, C. V. and Putnis, A. (2007) The effect of cation:anion ratio in solution on the
551 mechanism of barite growth at constant supersaturation: role of the desolvation process on
552 the growth kinetics. *Geochim. Cosmochim. Acta* **71**, 5168-5179.

553 Kucher, M., Babic, D., and Kind, M. (2006) Precipitation of barium sulfate: experimental
554 investigation about the influence of supersaturation and free lattice ion ratio on particle
555 formation. *Chem. Eng. Process.: Process Intensification* **45**, 900-907.

556 Kuwahara, Y. (2011) In situ atomic force microscopy study of dissolution of the barite (0 0 1)
557 surface in water at 30 °C. *Geochim. Cosmochim. Acta* **75**, 41-51.

558 Leininger, K. R., and Westley, J. (1968) The mechanism of the Rhodanese-catalyzed thiosulfate-
559 cyanide reaction. Thermodynamic and activation parameters. *J. Biol. Chem.* **243**, 1892-1899.

560 Lasaga, A. and Lütte, A. (2004) Mineralogical approaches to fundamental crystal crystal dissolution
561 kinetics. *Amer. Miner*. **89**, 527-540.

562 Li, Y. H. and Schoonmaker, J. E. (2003) Chemical Composition and mineralogy of marine
563 sediments. *Treatise on Geochemistry*, **7**, pp. 1-35.

564 Liu, S. T., Nancollas, G. H. and Gasiecki, E. A. (1976) Scanning electron microscopic and kinetic
565 studies of the crystallization and dissolution of barium sulfate crystals. *J. Crystal Growth* **33**,
566 11-20.

567 Mackay, E. J., Jordan, M. M. and Torabi, F. (2003) Predicting brine mixing deep within the
568 reservoir and its impact on scale control in marginal and deepwater developments. *Soc.*
569 *Petrol. Eng.* **SPE 85104**, 210-220.

570 Marchisio, D. L, Barresi, A. A. and Garbero, M. (2002) Nucleation, growth and agglomeration in
571 barium sulfate turbulent precipitation. *Amer. Inst. Chem. Eng. J.* **48**, 2039-2050.

572 Marini, L. (2007) Geological sequestration of carbon dioxide - Thermodynamics kinetics and
573 reaction path modeling. In *Development in Geochemistry* **11**. Elsevier, Amsterdam, The
574 Netherlands, pp. 1-453.

575 Matthis, A. L. and Erman, J. E. (1995) Cytochrome c peroxidase-catalyzed oxidation of yeast iso-1
576 ferrocytochrome c by hydrogen peroxide. Ionic strength dependence of the steady-state
577 parameters. *Biochemistry* **34**, 9985-9990.

578 Mealor, D. and Townshend, A. (1966) Homogeneous nucleation of some sparingly soluble salts.
579 *Talanta* **13**, 1069-1074.

580 Murphy, W. M. and Helgeson, H. C. (1987) Thermodynamic and kinetic constraints on reaction
581 rates among minerals and aqueous solutions. III. Activated complexes and the pH-
582 dependence of the rates of feldspar, pyroxene, wollastonite, and olivine hydrolysis. *Geochim.*
583 *Cosmochim. Acta* **51**, 3137-3153.

584 Murphy, W. M. and Helgeson, H. C. (1989) Thermodynamic and kinetic constraints on reaction
585 rates among minerals and aqueous solutions; IV, Retrieval of rate constants and activation
586 parameters for the hydrolysis of pyroxene, wollastonite, olivine, andalusite, quartz, and
587 nepheline. *Amer. J. Sci.* **289**, 17-101.

588 Murthy, M. S. (1994) Theory of crystal growth in phase transformations: precipitation of barium
589 sulphate. *Chem. Eng. Sci*. **49**, 2389 - 2393.

590 Nancollas, G. H. (1968) Kinetics of crystal growth from solution. *J. Crystal Growth* **3-4**, 335-339.

591 Nancollas, G. H. and Liu, S. T. (1975) Crystal growth and dissolution of barium sulfate. *Soc. Petrol.*
592 *Eng.* **SEP 5300**, 509-516.

593 Nancollas, G. H. and Purdie, N. (1963) Crystallization of barium sulphate in aqueous solutions.
594 *Trans. Faraday Soc.* **59**, 735-740.

595 Nielsen, A. E. (1958) The kinetics of crystal growth in barium sulfate precipitation. *Acta Chem.*
596 *Scand.* **12**, 951-958.

597 Nielsen, A. E. (1959) The kinetics of crystal growth in barium sulfate precipitation. II. Temperature
598 dependence and mechanism. *Acta Chem. Scand.* **13**, 784-802.

599 Nielsen, A. R. and Toft, J. M. (1984) Electrolyte crystal growth kinetics. *J. Crystal Growth* **67**, 278-
600 288.

601 Oelkers, E. H. (2001) General kinetic description of multioxide silicate mineral and glass
602 dissolution. *Geochim. Cosmochim. Acta* **65,** 3703-3719.

603 Oelkers, E. H. and Schott, J. (2005) Geochemical aspects of CO_2 sequestration. *Chem. Geo.* **217,**
604 183-186.

605 Oelkers, E. H., Schott, J. and Devidal J.-L. (1994) The effect of aluminum, pH, and chemical
606 affinity on the rates of aluminosilicate dissolution reactions. *Geochim. Cosmochim. Acta* **58**,
607 2011-2024.

608 Parkhurst, D. L. and Appelo, C. A. J. (2013) *Description of input and examples for PHREEQC.*
609 *Version 3–a computer program for speciation, batch-reaction, one-dimensional transport,*
610 *and inverse geochemical calculations.* U.S. Geological Survey Techniques. Methods Report,
611 book 6, chapter A43, pp. 1-497.

612 Paytan, A. and Griffith, E. M. (2007) Marine barite: Recorder of variations in ocean export
613 productivity. *Deep-Sea Res. Part II: Topical Studies in Oceanography* ***54***, 687-705.

614 Paytan, A., Averyt, K., Faul, K., Gray, E., and Thomas, E. (2007) Barite accumulation, ocean
615 productivity, and Sr/Ba in barite across the Paleocene–Eocene Thermal Maximum. *Geology*
616 **35**, 1139-1142.

617 Pedersen, A. O., Mensberg, K. L. D. and Kragh-Hansen, U. (1995) Effects of ionic strength and pH
618 on the binding of medium-chain fatty acids to human serum albumin. *Eur. J. Biochem.* **233**,

619 395-405.

620 Perlmutter-Hayman, B. and Persky, A. (1960) The influence of ionic strength and of temperature on
621 the rate of oxidation of D-glucose by bromine. *J. Amer. Chem. Soc.* **82**, 3809-3810.

622 Pham, V. T. H., Lu, P., Aagaard, P., Zhu, C., Hellevang, H. (2011) On the potential of CO_2-water-
623 rock interactions for CO_2 storage using a modified kinetic model. *Int. J. Greenhouse Gas*
624 *Contr.* **5,** 1002-1015.

625 Pina, C. M. (2009) Nanoscale dissolution and growth on anhydrite cleavage faces. *Geochim.*
626 *Cosmochim. Acta* **73**, 7034-7044.

627 Pina, C. M., Becker, U., Risthaus, P., Bosbach, D. and Putnis, A. (1998) Molecular-scale
628 mechanisms of crystal growth in barite. *Nature* **395,** 483-486.

629 Pina, C. M., Enders, M., Putnis, A. (2000) The composition of solid solutions crystallising from
630 aqueous solutions: the influence of supersaturation and growth mechanisms. *Chem. Geo*. **168**,
631 195-210.

632 Plummer, L. N., Parkhurst, D. L., Fleming, G. W. and Dunkle, S. A. (1988) *A computer program*
633 *incorporating Pitzer's equations for calculation of geochemical reactions in brines*. U.S.
634 Geological Survey Water Resources Investigations Report 88-4135, 208 pp.

635 Prieto, M. (2009) Thermodynamics of solid solution – aqueous solution systems. *Rev. Miner.*
636 *Geochem.* ***70***, 47-85.

637 Pruess, K., Yabusaki, S., Steefel, C., Lichtner, P. (2002) Fluid flow, heat transfer and solute
638 transport at nuclear storage tanks in the Hanford vadose zone. *Vadose Zone J.* **1,** 68-88.

639 Risthaus, P., Bosbach, D., Becker, U. and Putnis, A. (2001) Barite scale formation and dissolution
640 at high ionic strength studied with atomic force microscopy. *Colloids Surfaces A:*
641 *Physicochem. Eng. Aspects* **191**, 201-214.

642 Rizkalla, E. N. (1983) Kinetics of the crystallization of barium sulphate. *J. Chem. Soc. Faraday*
643 *Trans. 1: Phys. Chem. Condensed Phases* **79**, 1857-1867.

644 Ruiz-Agudo, C., Putnis, C. V., Ruiz-Agudo, E., Putnis, A. (2015) The influence of pH on barite
645 nucleation and growth. *Chem. Geo*. **391**, 7-18.

646 Saldi, G. D., Jordan, G., Schott, J. and Oelkers, E. H. (2009) Magnesite growth rates as a function
647 of temperature and saturation state. *Geochim. Cosmochim. Acta* **73**, 5646-5657.

648 Saldi, G. D., Schott, J., Pokrovsky, O. S., Gautier, Q. and Oelkers, E. H. (2012) An experimental
649 study of magnesite precipitation rates at neutral to alkaline conditions and 100–200 °C as a
650 function of pH, aqueous solution composition and chemical affinity. *Geochim. Cosmochim.*
651 *Acta* **83**, 93-109.

652 Schott J. and Oelkers E. H. (1995) Dissolution and crystallization rates of silicate minerals as a
653 function of chemical affinity. *Pure App. Chem.* **67**, 903-910.

654 Schott, J., Pokovsky, O. S. and Oelkers, E. H. (2009) The link between mineral
655 dissolution/precipitation kinetics and solution chemistry. *Rev. Mineral. Geochem.* **70**, 207-
656 258.

657 Schott, J., Oelkers, E. H., Bénézeth, P., Goddéris, Y., François, L. (2012) Can accurate kinetic laws
658 be created to describe chemical weathering? *C. R. Geoscience* **344**, 568-585.

659 Shindo, H., Kaise, M., Kondoh, H., Nishihara, C., Nozoye, H. (1992) Crystal faces of anhydrite
660 ($CaSO_4$) and their preferential dissolution in aqueous solutions studied with AFM. *Appl. Surf.*
661 *Sci.* **60**(6), 491-497.

662 Sorbie, K. S. and Mackay, E. J. (2000) Mixing of injected, connate and aquifer brines in
663 waterflooding and its relevance to oilfield scaling. *J. Petrol. Sci. Eng.* **27**, 85-106.

664 Steyer, C. and Sundmacher, K. (2009) Impact of feeding policy and ion excess on particle shape in
665 semi-batch precipitation of barium sulfate. *J. Crystal Growth* **311**, 2702-2708.

666 Symeopoulos; B. D. and Koutsoukos, P. G. (1992) Spontaneous Precipitation of barium sulfate in
667 aqueous solution. *J. Chem. Soc. Faraday Trans.* **88**, 3063-3066.

668 Taguchi, K., Garside, J., and Tavare, N. S. (1996) Nucleation and growth kinetics of barium
669 sulphate in batch precipitation. *J. Crystal Growth* **163**, 318-328.

670 Tang, R., Nancollas, G. H. and Orme, C. A. (2001) Mechanism of dissolution of sparingly soluble
671 electrolytes. *J. Amer. Chem. Soc.* **123**, 5437-5443.

672 Temkin, M. I. (1963) The kinetics of stationary reactions. *Akad, Nauk SSR Doklady* **152**, 782-785.

673 Tsukahara, K. (1986) Ionic strength effect on the ascorbate reduction of sperm whale and horse
674 heart metmyoglobins. *Inorg. Chim. Acta* **124**, 199-202.

675 van der Leeden, M. C., Kashchiev, D. and van Rosmalen, G. M. (1992) Precipitation of barium
676 sulfate: induction time and the effect of an additive on nucleation and growth. *J. Colloid*
677 *Interface Sci.* **152**, 338-350.

678 Verma, A., Pruess, K. (1988) Thermohydrological conditions and silica redistribution near high-
679 level nuclear wastes emplaced in saturated geological formations. *J. Geophys. Res. – Solid*
680 *Earth* **93,** 1159-1173.

681 Vetter, O. J., Kandarpa, V. and Harouaka, A. (1982) Prediction of scale problems due to injection of
682 incompatible waters. *J. Petrol. Technology* **34**, 273-284.

683 Walton, A. G. (1963) The nucleation of sparingly soluble salts from solution. *Anal. Chim. Acta* **29**,
684 434-441.

685 Walton, G. and Walden, G. H. Jr. (1946). The contamination of precipitated barium sulfate by
686 univalent cations. *J. Amer. Chem. Soc.* **68**, 1742-1950.

687 Wat, R. M. S., Sorbie, K. S., Todd, A. C., Ping, C., and Ping, J. (1992) Kinetics of $BaSO_4$ crystal
688 growth and effect in formation damage. *Soc. Petrol. Eng.* **SPE 23814**, 429-437.

689 Wolgemuth, K. and Broecker, W.S. (1970) Barium in sea water. *Earth Planet. Sci. Lett.* **8**, 372-378.

690 Wong, D. C. Y., Jaworski, Z. and Nienow, A. W. (2001) Effect of ion excess on particle size and
691 morphology during barium sulphate precipitation: an experimental study. *Chem. Eng. Sci.* **56**,
692 727-734.

693 Wood, J. M. (1973). Effect of ionic strength on the activity of carnitine palmityltransferase I.
694 *Biochemistry **12***, 5268-5273.

695 Xu, T., Apps, J. A., and Pruess, K. (2005) Mineral sequestration of carbon dioxide in a sandstone-
696 shale system. *Chem. Geo*. **217,** 295-318.

Zhang, L., Soong, Y., Dilmore, R., Lopano, C. (2015) Numerical simulation of porosity ad permeability evolution of Mount Simon sandstone under geological carbon sequestration conditions. *Chem. Geo.* **403**, 1-12.

9. Supplementary materials

Figure A. Barite dissolution and precipitation rates calculated as a function of saturation state using Eqn. 5 and the parameters provided in Table 2 at 60 °C, in solutions containing (a) 0, (b) 0.1, (c) 1, and (d) 1.5 mol kg^{-1} NaCl. Circles represent the dissolution rate and diamonds, the precipitate rate. Solid lines correspond to the slope of the rates; the dashed lines show the position of equilibrium and zero net rate.

Figure B. The same as Figure A, but for experiments at 25 °C and containing (a) 10^{-3} mol kg^{-1} Ca in NaCl free solution, (b) 10^{-3} mol kg^{-1} Ca in 1 mol kg^{-1} NaCl; (c) 10^{-5} mol kg^{-1} Sr in NaCl free solution and (d) 10^{-5} mol kg^{-1} Sr in 1 mol kg^{-1} NaCl; (e) 0.06 mol kg^{-1} Mg in 1 mol kg^{-1} NaCl.

Figure Captions

Figure 1. Scanning electron microscope (SEM) images of barite before and after reaction. (a) The original, natural barite seed crystals; (b) after dissolution in 1.0 mol kg^{-1} aqueous NaCl solution at 25 °C and initial pH of 5.93, from Experiment DC; (c) after precipitation in 1.0 mol kg^{-1} aqueous NaCl solutions at 25 °C, where pH was 3, from Experiment 2A; (d) after dissolution in 1.0 mol kg^{-1} aqueous NaCl solutions at 25 °C and pH 10, from Experiment 2H; (e) after dissolution of 0.1 g of barite, from Experiment 2B; and (f) after precipitation in experiment 2PD performed in an aqueous solution with initial Ba:SO_4 mole ratio of 1:64.

Figure 2. Temporal evolution of Ba concentration during the closed system barite dissolution (a) 1K, 2K, 3K and precipitation (a) 1PK, 2PK, and 3PK experiments, which were performed at 25 °C in 1.0 mol kg^{-1} NaCl solutions at the indicated reactor shaking rates, and precipitation experiments (b and c) UA3, UA5, UA10, SA3, SA5 and SA10 performed at 25 °C in 0.1 mol kg^{-1} NaCl solutions (b) in the absence and (c) in the presence of barite seed crystals. Analytical uncertainty in the measurements is approximately equal to the symbol size.

Figure 3. The change in Ba concentration during the dissolution and precipitation in experiments at 25 °C, as a function of ionic strength (a) 0, (b) 0.1, (c) 1 and (d) 1.5 mol kg^{-1} aqueous NaCl; and at 60 °C in (e) 0.1, (f) 0.7, (g) 1, and (h) 1.5 mol kg^{-1} aqueous NaCl. The symbols correspond to measured aqueous Ba concentration and the solid curves were determined using Eqn. 5 and the regression parameters from Table 2 and reaction order, n' = 1 for precipitation and 0.2 for dissolution. The dashed lines represent the measured equilibrium aqueous Ba concentration. Analytical uncertainty is approximately equal to the symbol size.

Figure 4. Change in aqueous Ba concentration during barite dissolution experiments at 90 °C in NaCl solutions of 0.1, 0.7, 1.0 and 1.5 mol kg^{-1}. The symbols correspond to measured Ba concentration and the solid curves were determined using Eqn. 5 with the regression parameters from Table 2 and reaction order, n' = 0.2. Analytical uncertainty is approximately the size of the symbols.

Figure 5. Aqueous Ba concentration during barite dissolution at 25°C, in 1 mol kg^{-1} aqueous NaCl solutions at pH 2, 3, 6.5, 9 and 10.

Figure 6. Aqueous barium concentration change with time during barite dissolution as a function of initial barite mass (0.1 g, 0.5 g and 1.0 g), thus surface area, at 25 °C in 1 mol kg^{-1} NaCl solutions, at pH 6.65.

Figure 7. Evolution of aqueous barium concentration during closed system dissolution and precipitation at 25 °C, in solutions containing other divalent cations: (a) 10^{-3} mol kg^{-1} Ca in NaCl free solution, (b) 10^{-3} mol kg^{-1} Ca in 1 mol kg^{-1} NaCl; (c) 0.06 mol kg^{-1} Mg in NaCl free solution, dissolution only; (d) 0.06 mol kg^{-1} of Mg in 1 mol kg^{-1} NaCl; (e) 10^{-5} mol kg^{-1} Sr in NaCl free solution and (f) 10^{-5} mol kg^{-1} Sr in 1 mol kg^{-1} NaCl.

Figure 8. Aqueous Ba concentration during barite precipitation at 25 °C in solutions where supersaturation state is the same but Ba:SO_4 mole ratio varied: 1:64, 1:16 and 1:4.

Figure 9. The best fit for the time dependent change of aqueous Ba concentration during dissolution at (a) 25 °C in NaCl free solution (Experiment DD) and (b) at 60 °C in a solution containing 1 mol kg^{-1} NaCl solution (Experiment 2J). The solid and dashed curves are based on the bet fit of the first 5 measured concentrations by adopting the overall reaction orders of 2, 1 and 0.2 with respect to barite saturation state. Analytical uncertainty is approximately equal to the symbol size.

754 **Figure 10**. Dissolution and precipitation rate constants as a function of ionic strength from
755 experiments at (a) 25, (b) 60, and (c) 90 °C. The symbols represent the derived rate constants and
756 the curves correspond to linear fits to the data.

757 **Figure 11.** The correlation of barite dissolution rate constants with pH at 25 °C in 1 molal NaCl
758 solutions. Uncertainty is ~0.1 of a logarithm unit.

759 **Figure 12**. Arrhenius plots for barite dissolution rates measured in NaCl solutions: (a) 0.1, (b) 1.0,
760 and (c) 1.5 mol kg^{-1}.

761 **Figure 13**. Comparison of the rate constants normalised to geometric surface area with those
762 measured in this study and presented in Table 2.

763 **Figure 14.** Barite dissolution and precipitation rates as a function of saturation state, derived using
764 Eqn. 5 and the parameters provided in Table 2 at 25 °C, in solutions of (a) 0, (b) 0.1, (c) 1 and (d)
765 1.5 mol kg^{-1} NaCl. Circles represent the dissolution rate and diamonds, the precipitation rate. There
766 is no discontinuity between the two at the equilibrium state. Solid lines correspond to the slope of
767 the rates; the dashed lines show the position of equilibrium and zero net rate.

Table 1. Composition of the initial fluids used in the closed system, barite dissolution and precipitation experiments.

Exp.[1]	T[1] (°C)	Process[1]	Initial reactive fluid composition (mol kg^{-1})								Initial pH	Initial barite mass (g)
			NaCl	$BaCl_2 \cdot 2H_2O$ x10^{-4}	Na_2SO_4 x10^{-4}	$CaCl_2 \cdot 2H_2O$ x10^{-3}	$MgCl_2 \cdot 6H_2O$ x10^{-2}	$SrCl_2 \cdot 6H_2O$ x10^{-5}	HCl x10^{-4}	NH_4Cl x10^{-3}	NH_4OH x10^{-4}		
UA3	25	P	0.1	0.97	0.97				0.84			3.80	0
UA5	25	P	0.1	1.38	1.67				1.20			3.63	0
UA10	25	P	0.1	3.07	3.35				2.66			3.26	0
SA3	25	P	0.1	0.98	1.01				0.85			3.75	0.52
SA5	25	P	0.1	1.61	1.61				1.39			3.54	0.52
SA10	25	P	0.1	3.35	3.25				2.91			3.22	0.51
DD	25	D	0.0									5.97	0.52
DA	25	D	0.1									6.10	0.56
DC	25	D	1.0									5.93	0.53
DB	25	D	1.5									6.13	0.51
1A	25	P	0.0	0.55	0.51				0.47			4.17	0.51
2A	25	P	1.0	5.03	4.92				3.98			2.92	0.50
3A	25	P	1.5	5.54	5.99				4.89			2.75	0.51
4J	60	D	0.1									4.67	0.50
5J	60	D	0.7									4.61	0.51
2J	60	D	1.0									4.51	0.50
3J	60	D	1.5									4.49	0.51
4PJ	60	P	0.1	2.40	2.44							4.73	0.50
5PJ	60	P	0.7	6.10	6.09							4.53	0.51
2PJ	60	P	1.0	7.32	7.25							4.55	0.50
3PJ	60	P	1.5	8.58	8.57							4.50	0.50
HA	90	D	0.1									5.21	0.57
W	90	D	0.7									NM	0.51
HB	90	D	1.0									3.08	0.55
HC	90	D	1.5									3.13	0.55
2E	25	D	1.0						100			2.00	0.50
2F	25	D	1.0						10			2.99	0.51
2G	25	D	1.0							9.90	0.21	8.96	0.50
2H	25	D	1.0							9.70	5.70	10.01	0.50
2B	25	D	1.0									6.62	0.10
2C	25	D	1.0									6.64	0.50
2D	25	D	1.0									6.67	1.00
1Ca	25	D	0.0			1.12						5.35	0.55
2Ca	25	D	1.0			1.13						6.46	0.53
1Mg	25	D	0.0				6					5.46	0.52
2Mg	25	D	1.0				6					6.49	0.50
1S	25	D	0.0					1.03	0.86			3.49	0.50
2Sr	25	D	1.0					1.03	0.86			3.34	0.50
1PC	25	P	0.0	0.54	0.53	1.01						5.67	0.51
2PC	25	P	1.0	4.52	4.44	1.01						5.94	0.50
1PM	25	P	0.0	0.54	0.54		6					5.61	0.51
2PM	25	P	1.0	4.55	4.49		6					6.27	0.50
1PS	25	P	0.0	0.54	0.53			1.03	0.86			3.65	0.51
2PS	25	P	1.0	4.54	4.50			1.03	0.86			3.36	0.50
2PA	25	P	1.0	2.33	9.39							6.10	0.51
2PB	25	P	1.0	1.31	20.98							6.13	0.50
2PD	25	P	1.0	0.59	37.65							6.08	0.50
1K	25	D	1.0									3.79	0.50
2K	25	D	1.0									3.76	0.50
3K	25	D	1.0									4.95	0.50
1PK	25	P	1.0	4.66	4.67							4.95	0.50
2PK	25	P	1.0	4.66	4.67							3.95	0.50
3PK	25	P	1.0	4.66	4.67							3.89	0.50

1) Exp.: experiment name; T: temperature; D: dissolution; P: precipitation; NM: not measured.

Table

Table 2. Rate parameters for barite dissolution and precipitation, determined from closed system experiments; n' = 0.2 for dissolution and n' = 1 for precipitation.

Exp.[1]	T[1] (°C)	NaCl (mol kg^{-1})	Variable	Rate constant, normalised by geometric surface area (mol m^{-2} s^{-1})			Rate constant, normalised by BET surface area (mol m^{-2} s^{-1})		
				log k_D	log k_P	calculated log k_D	log k_D	log k_P	calculated log k_D
DD; 1A	25	0		-7.30	-8.46	-7.34	-8.05	-9.20	-8.10
DA; SA5	25	0.1		-6.49	-7.62	-7.15	-7.24	-8.37	-7.91
DC; 2A	25	1.0		-6.42	-7.60	-6.74	-7.17	-8.35	-7.50
DB; 3A	25	1.5		-6.35	-7.55	-6.61	-7.10	-8.30	-7.37
4J; 4PJ	60	0.1		-6.60	-7.22	-6.65	-7.35	-7.97	-7.41
5J; 5PJ	60	0.7		-6.28	-6.60	-6.34	-7.03	-7.35	-7.10
2J; 2PJ	60	1.0		-6.17	-6.54	-6.23	-6.92	-7.29	-7.00
3J; 3PJ	60	1.5		-6.10	-6.52	-6.10	-6.85	-7.27	-6.86
HA	90	0.1		-6.30		-6.34	-7.05		-7.10
W	90	0.7		-6.00		-5.97	-6.75		-6.73
HB	90	1.0		-5.89		-5.87	-6.64		-6.63
HC	90	1.5		-5.80		-5.74	-6.54		-6.50
2E	25	1.0	pH = 2	-6.64		-6.62	-7.39		-7.38
2F	25	1.0	pH = 3	-6.49		-6.65	-7.24		-7.41
2C	25	1.0	pH = 6.5	-6.35		-6.75	-7.10		-7.51
2G	25	1.0	pH = 9	-6.89		-6.83	-7.64		-7.59
2H	25	1.0	pH = 10	-6.82		-6.86	-7.57		-7.62
2B	25	1.0	0.1 g[a]	-6.35		-6.76	-7.10		-7.52
2C	25	1.0	0.5 g[a]	-6.35		-6.76	-7.10		-7.52
2D	25	1.0	1.0 g[a]	-6.60		-6.76	-7.35		-7.52
1Ca; 1PC	25	0	$Ca^{2+} = 10^{-3}$ m	-7.35	-8.22	-7.29	-8.10	-8.97	-8.05
2Ca; 2PC	25	1.0	$Ca^{2+} = 10^{-3}$ m	-6.49	-7.35	-6.75	-7.24	-8.10	-7.51
1Mg	25	0	Mg^{2+} = 0.06 m	-6.96		-7.12	-7.71		-7.88
1PC	25	0	Mg^{2+} = 0.06 m	-6.46		-7.12	-7.20		-7.88
2Mg; 2PM	25	1.0	Mg^{2+} = 0.06 m	-6.48	-7.40	-6.72	-7.23	-8.15	-7.48
1S; 1PS	25	0	$Sr^{2+} = 10^{-5}$ m	-7.00	-8.40	-7.26	-7.82	-8.97	-8.02
2Sr; 2PS	25	1.0	$Sr^{2+} = 10^{-5}$ m	-6.40	-7.30	-6.66	-7.15	-8.05	-7.42
2A	25	1.0	$Ba:SO_4$ = 1:1[b]		-7.60	*-7.56*		-8.35	*-8.32*
2PA	25	1.0	$Ba:SO_4$ = 1:4[b]		-7.60	*-6.56*		-8.35	*-7.32*
2PB	25	1.0	$Ba:SO_4$ = 1:16[b]		-7.82	*-6.56*		-8.57	*-7.32*
2PD	25	1.0	$Ba:SO_4$ = 1:64[b]		-7.77	*-6.56*		-8.52	*-7.32*
1K; 1PK	25	1.0	0.2 cycle s^{-1}	-7.10	-7.48	-6.67	-7.85	-8.23	-7.42
2K; 2PK	25	1.0	1.3 cycles s^{-1}	-6.77	-7.40	-6.71	-7.52	-8.15	-7.46
3K; 2PK	25	1.0	2.8 cycles s^{-1}	-6.15	-6.85	-6.68	-6.90	-7.60	-7.43

1) Exp.: Experiment name; T: temperature; m: mol kg^{-1}; log k_D: logarithm of the rate constant for dissolution; log k_P: logarithm of the rate constant for precipitation; [a] : initial barite mass; [b]: mole ratio of Ba to SO_4 of the initial solutions; *italics*: extrapolated to the logarithm of the rate constant for precipitation using the activation energy for dissolution.

Figure 1

Click here to download high resolution image

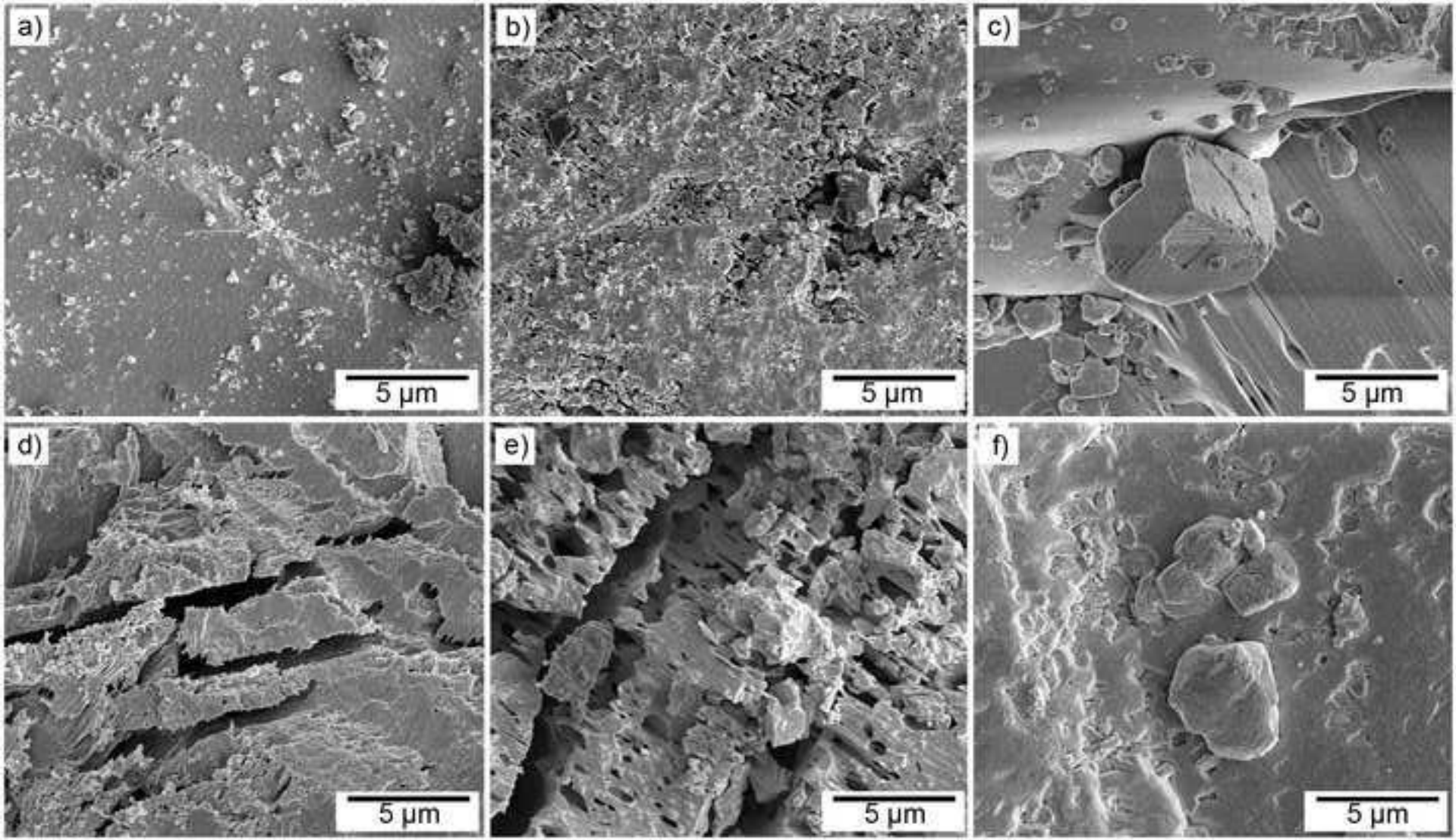

Figure 2

Click here to download high resolution image

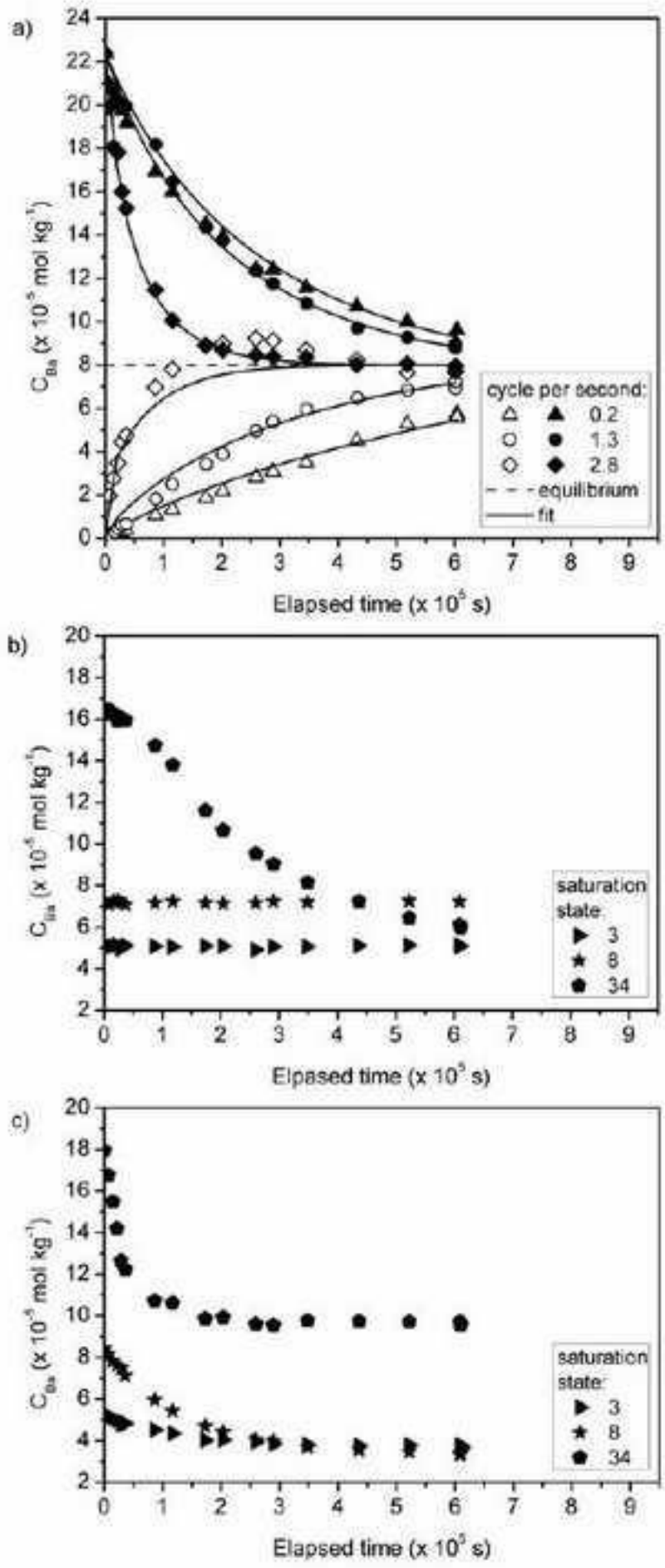

Figure 3

Click here to download high resolution image

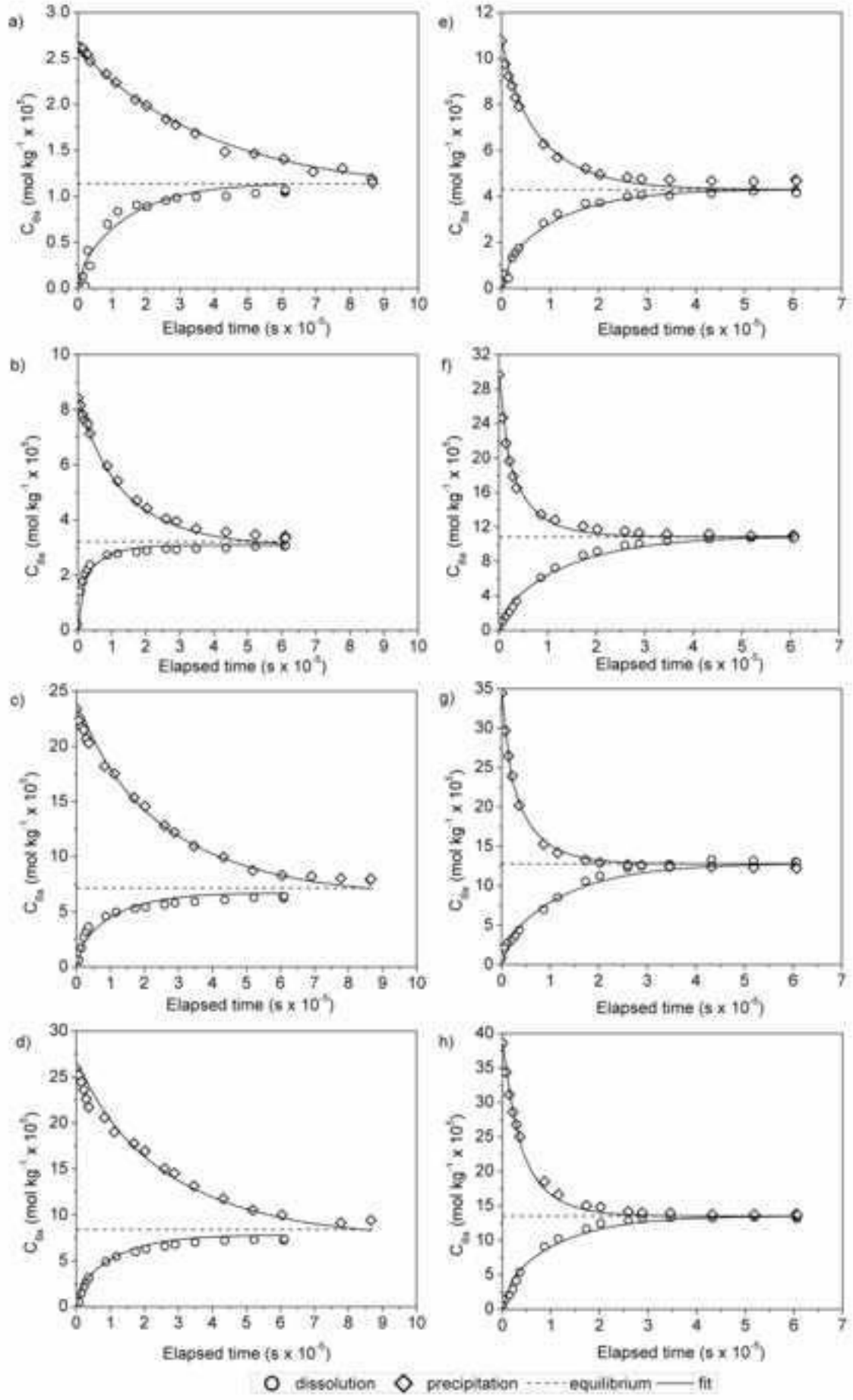

Figure 4

Click here to download high resolution image

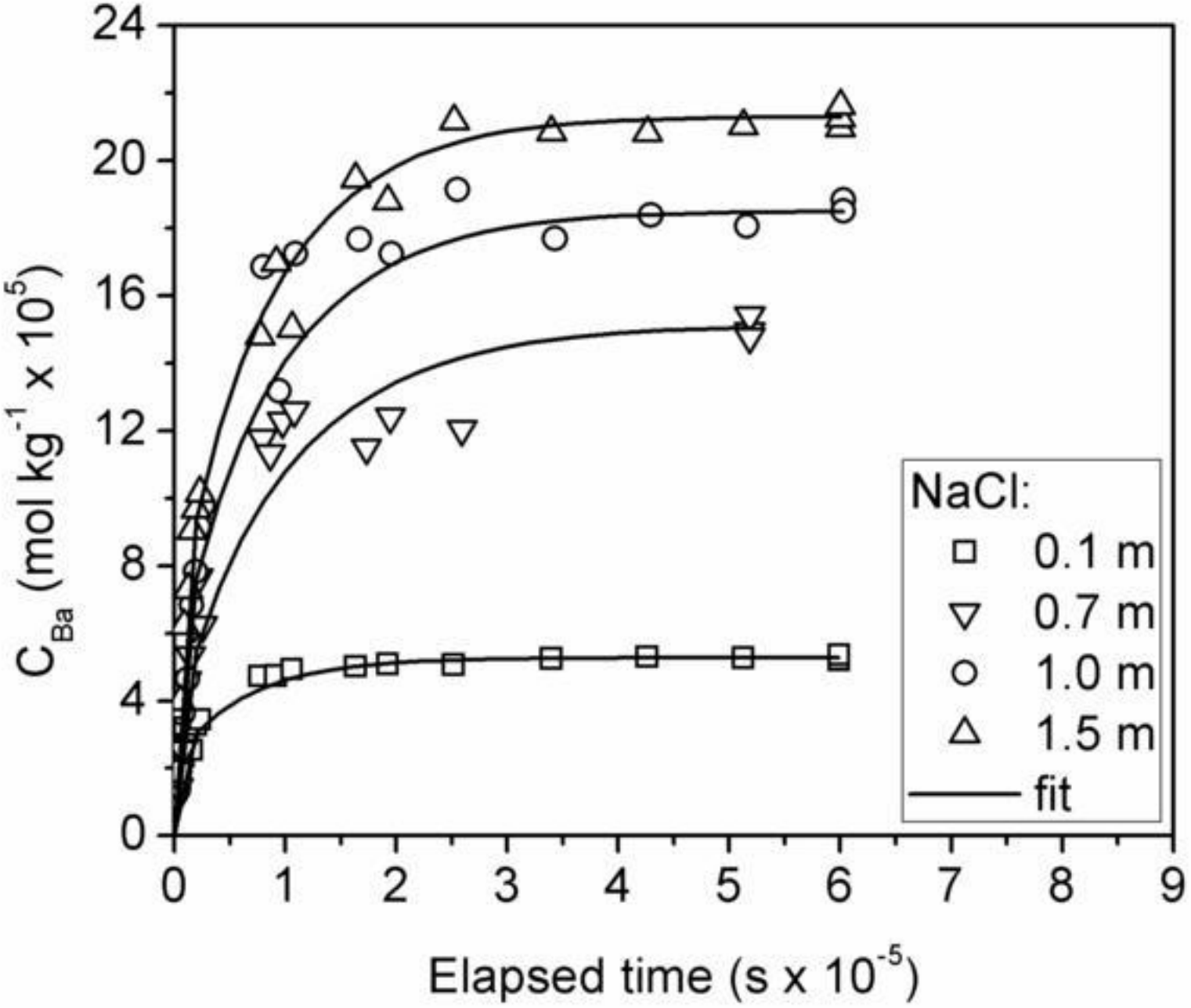

Figure 5

Click here to download high resolution image

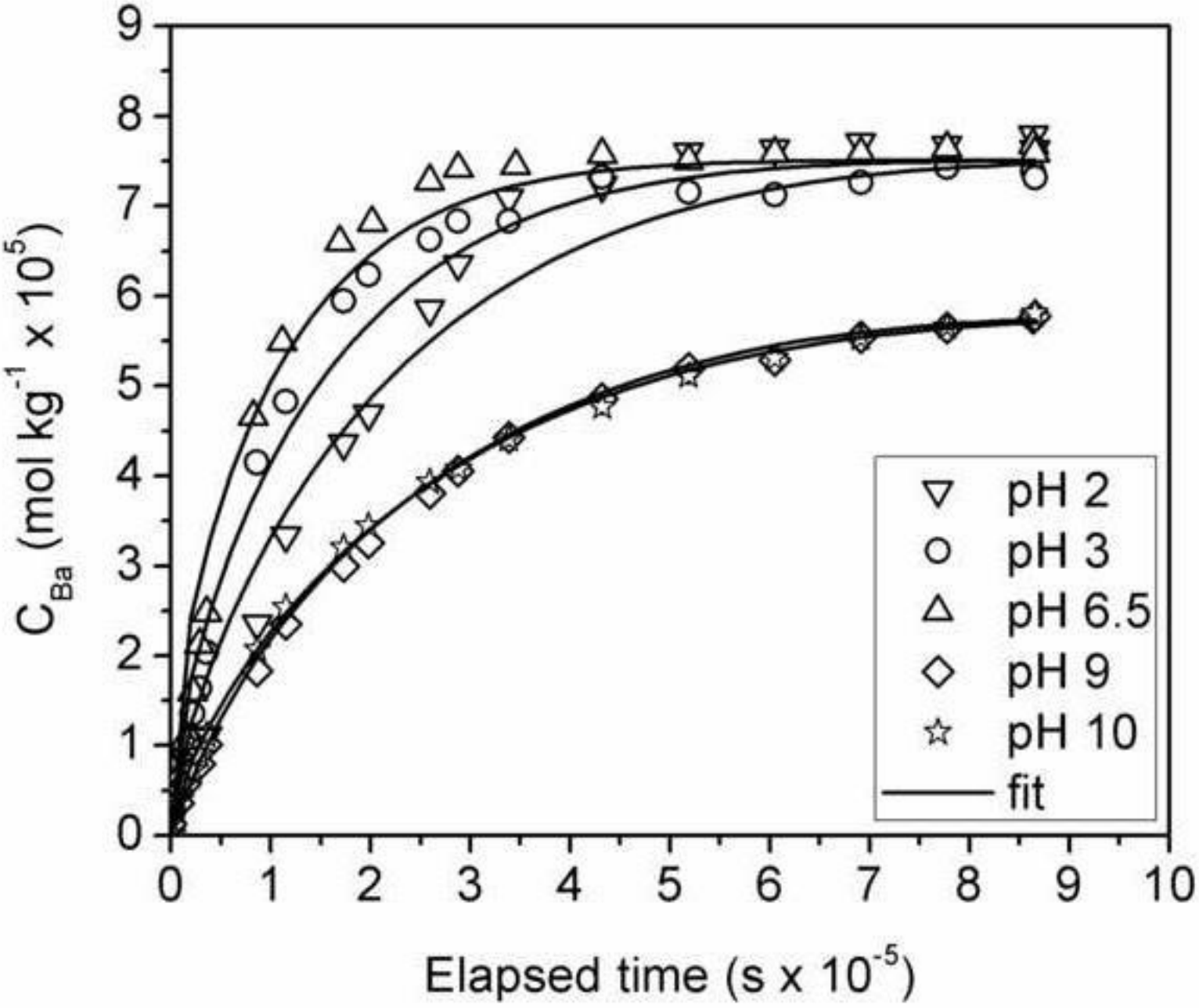

Figure 6

Click here to download high resolution image

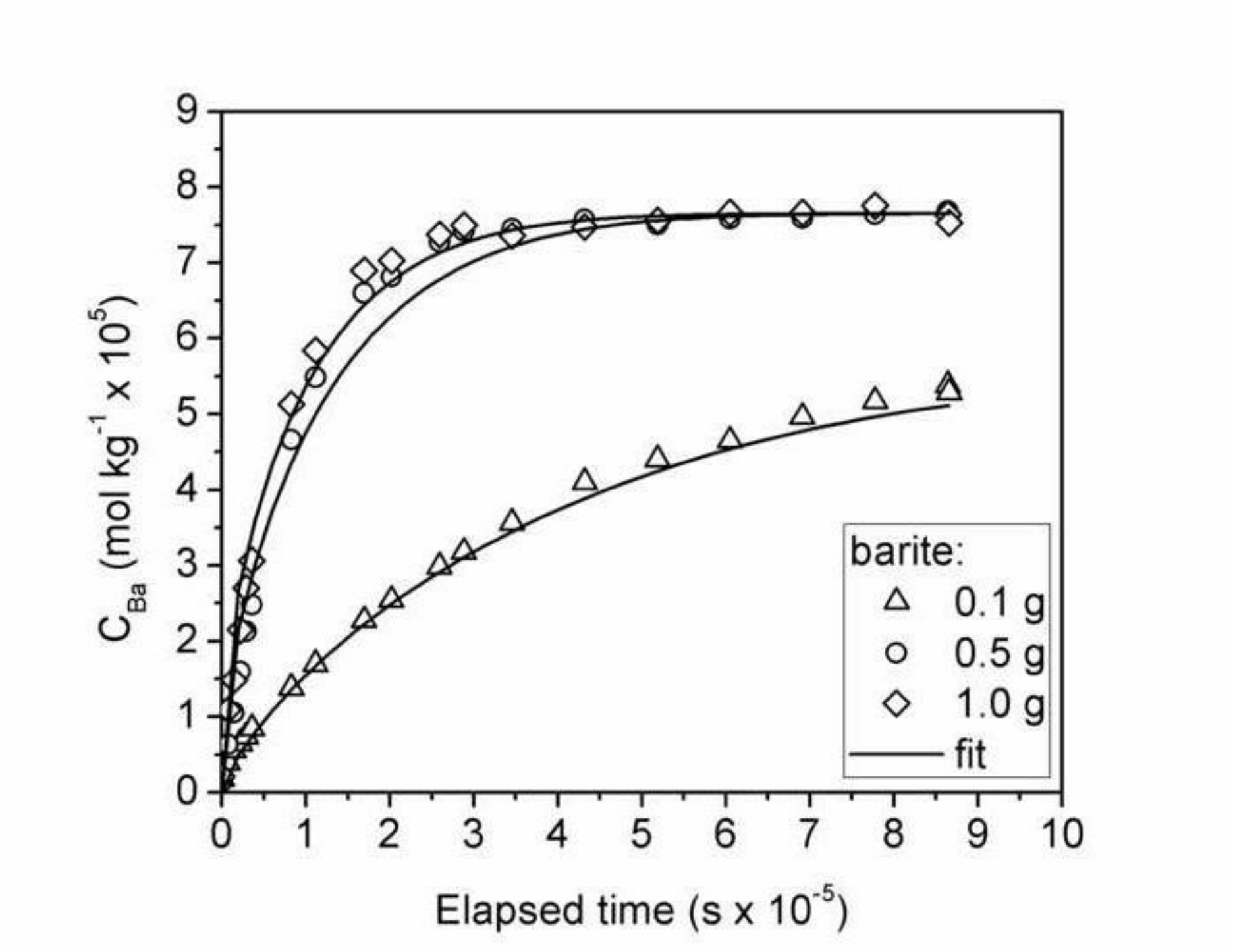

Figure 7

Click here to download high resolution image

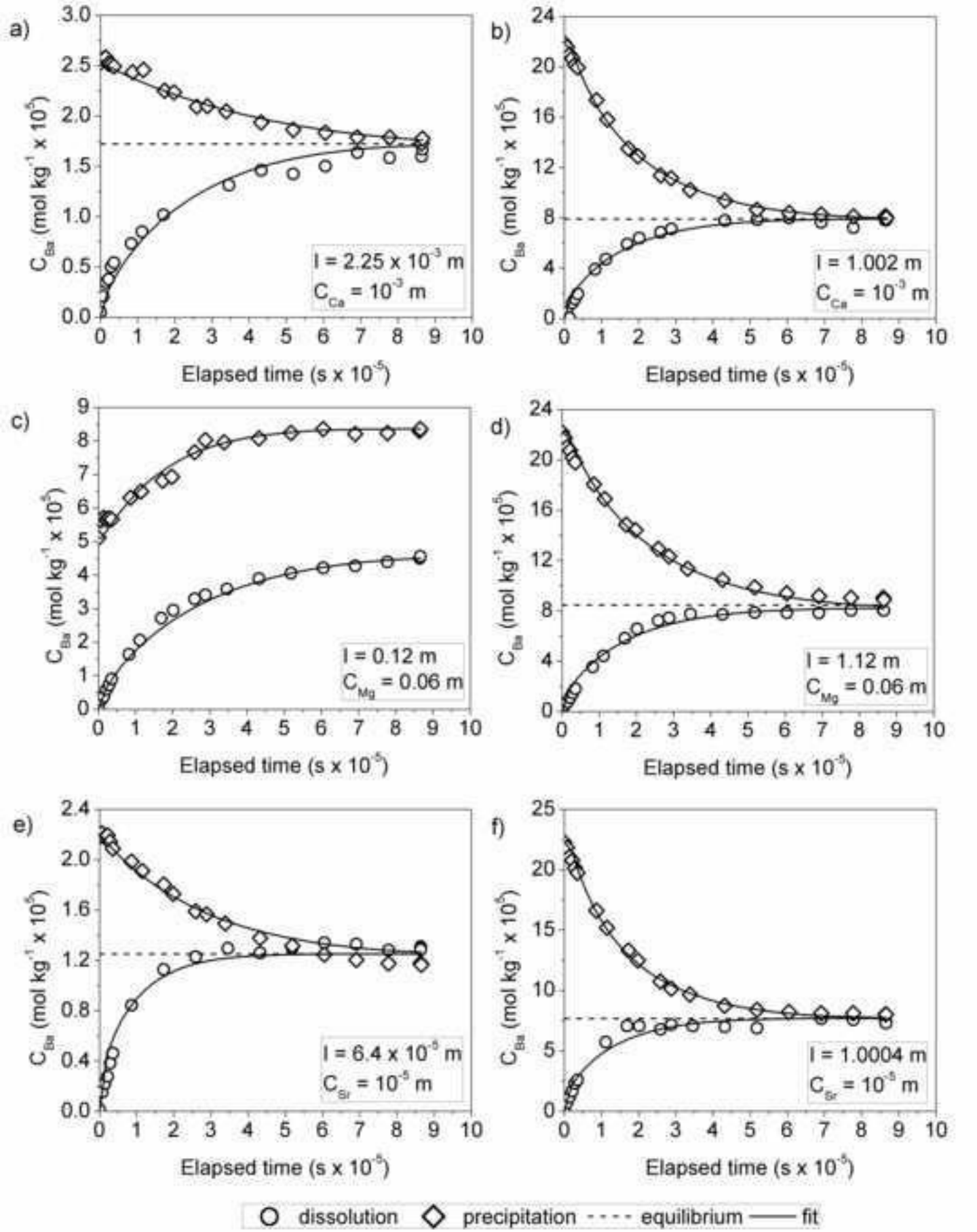

Figure 8

Click here to download high resolution image

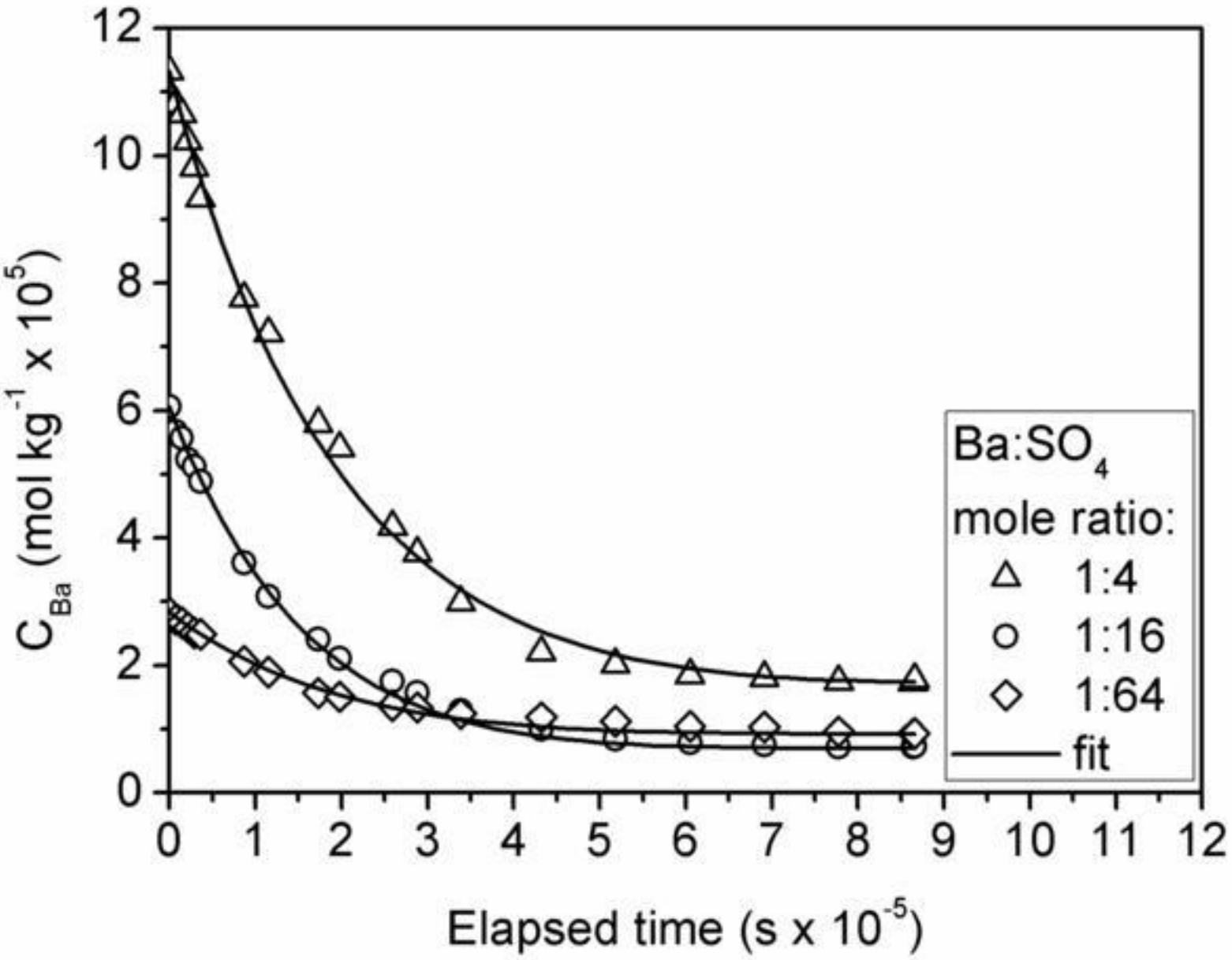

Figure 9

Click here to download high resolution image

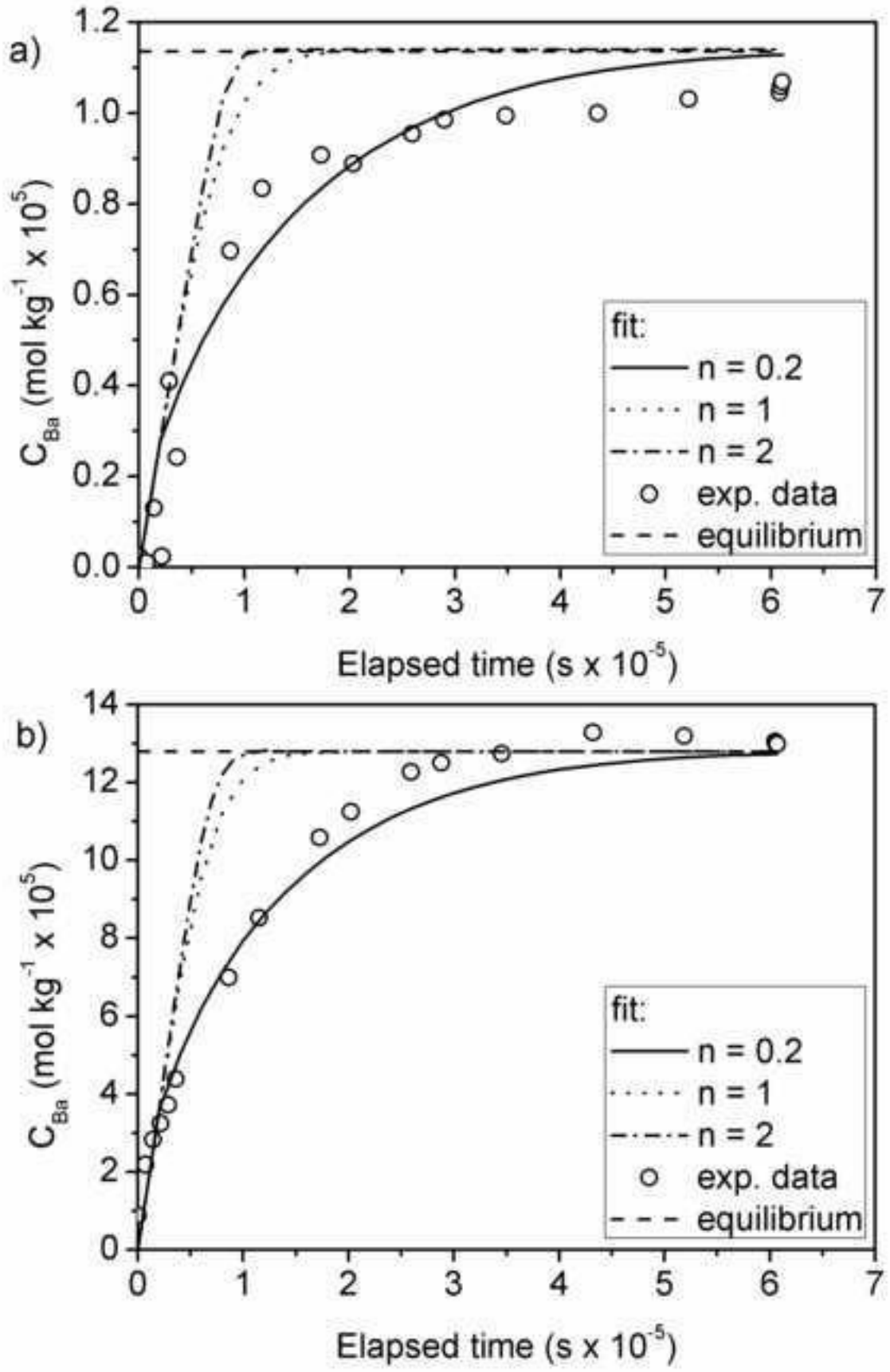

Figure 10

Click here to download high resolution image

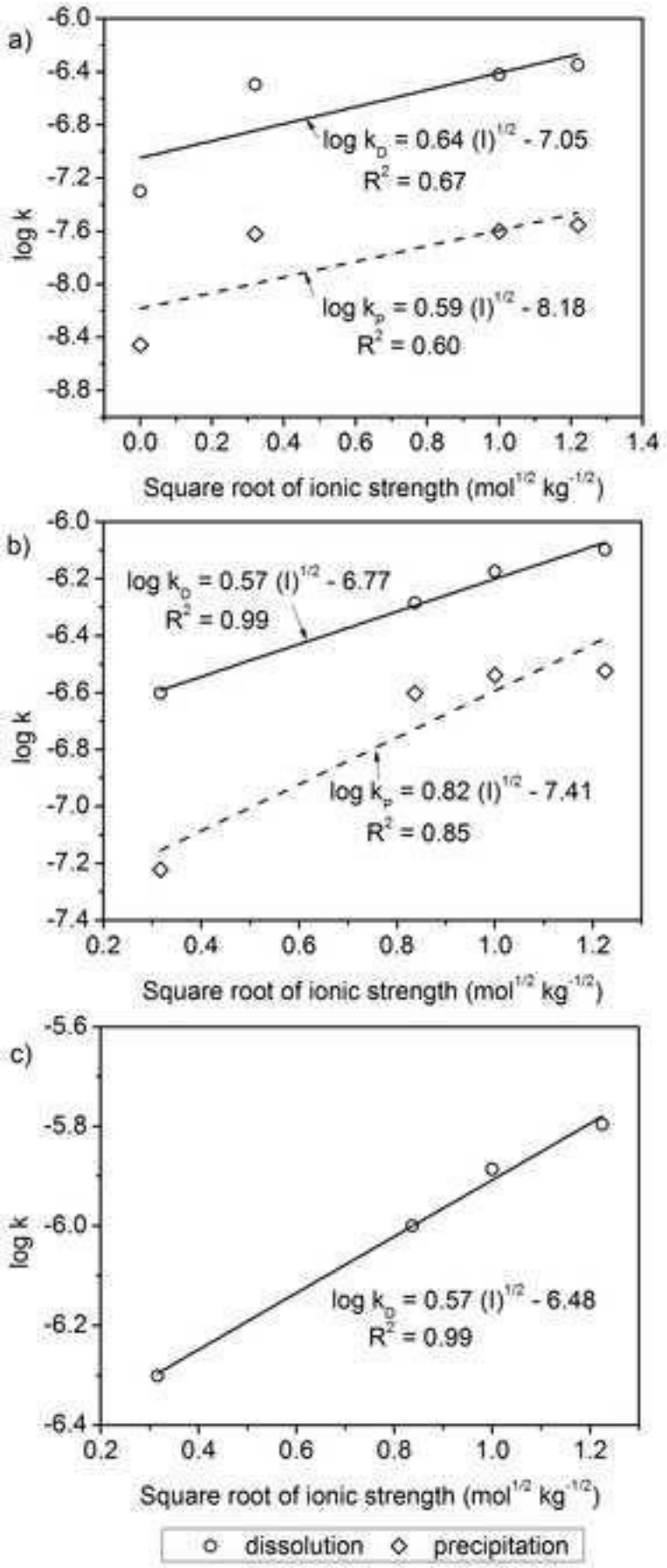

Figure 11

Click here to download high resolution image

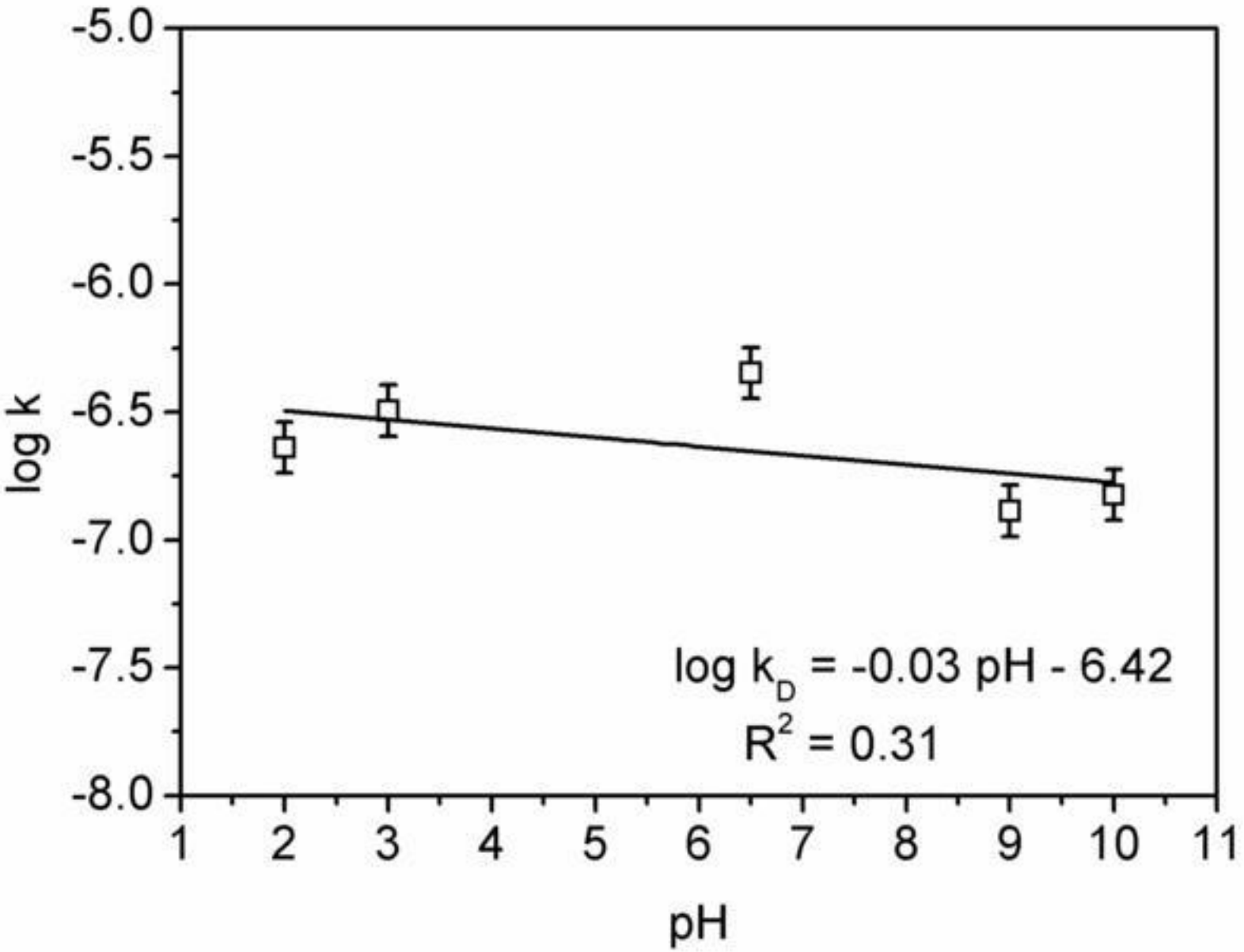

Figure 12

Click here to download high resolution image

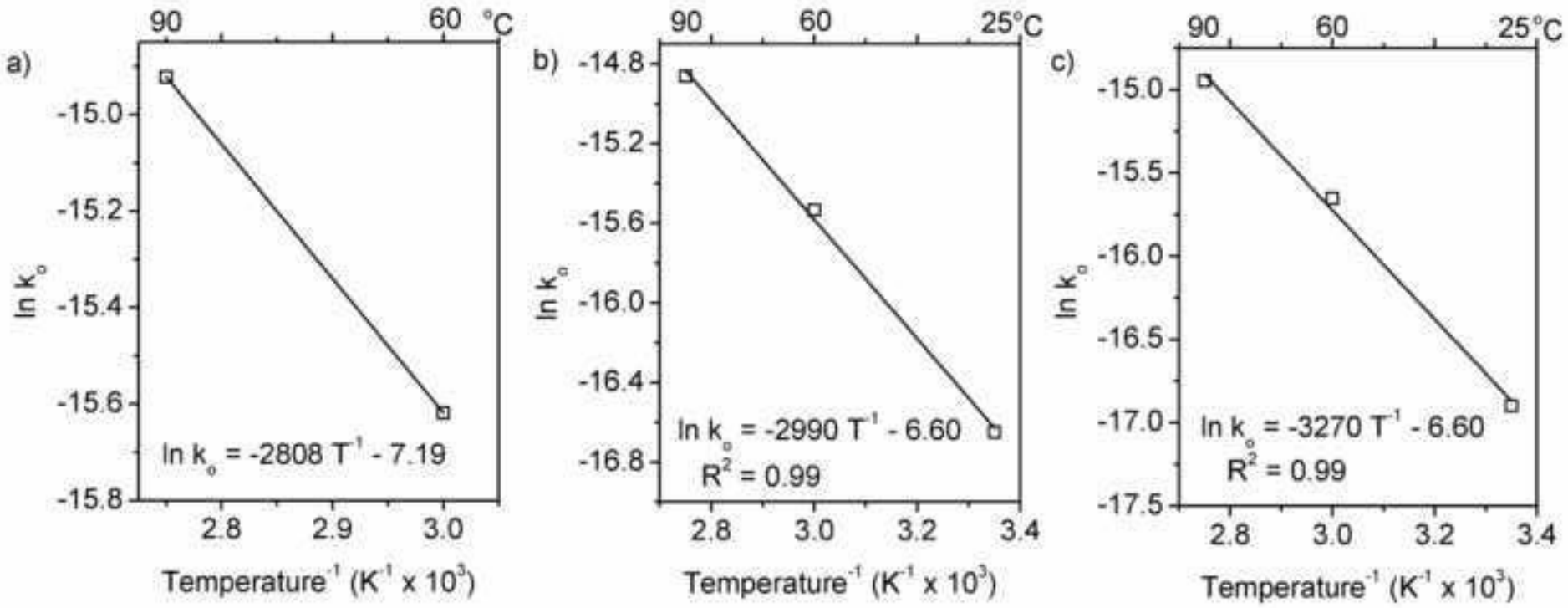

Figure 13

Click here to download high resolution image

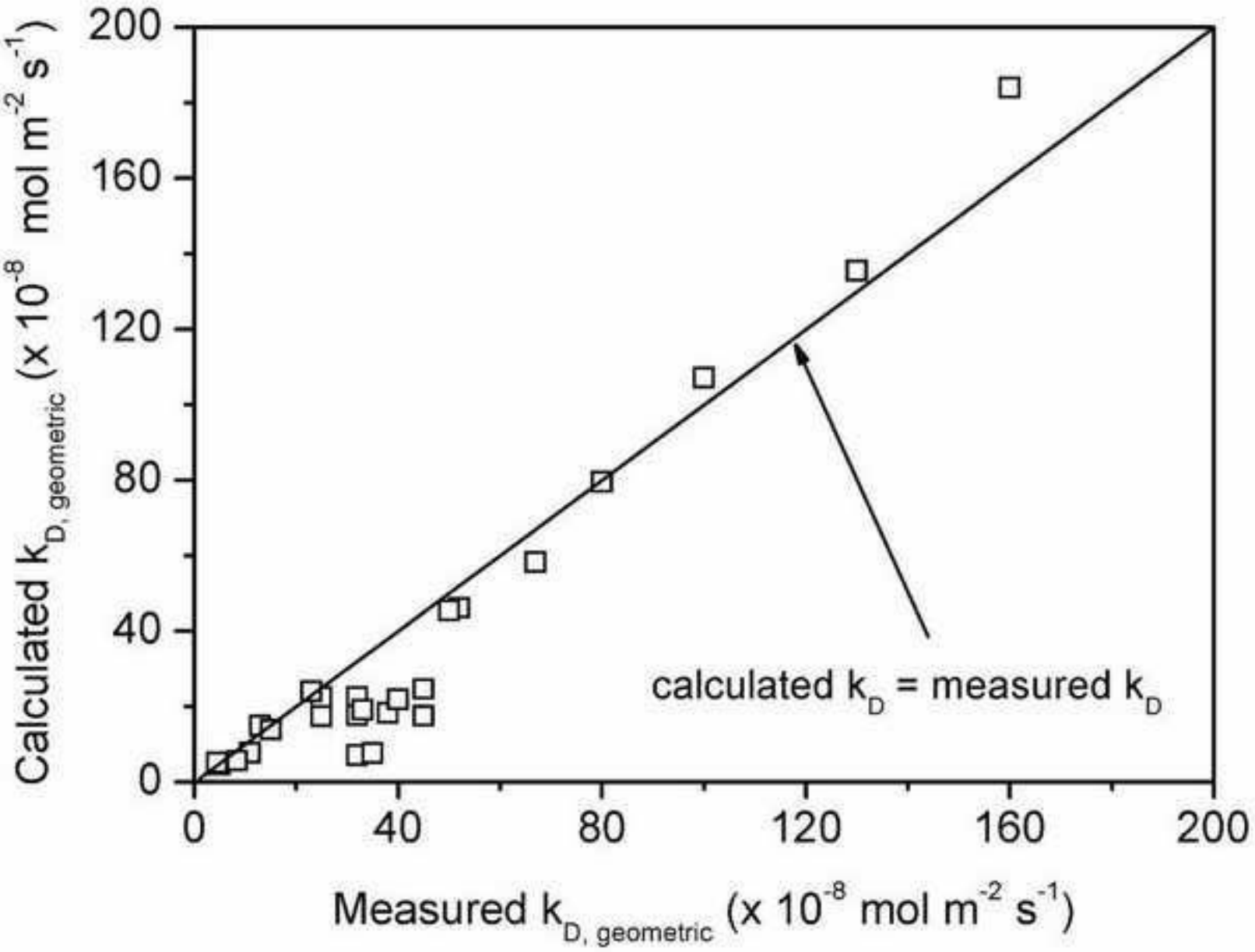

Figure 14

Click here to download high resolution image

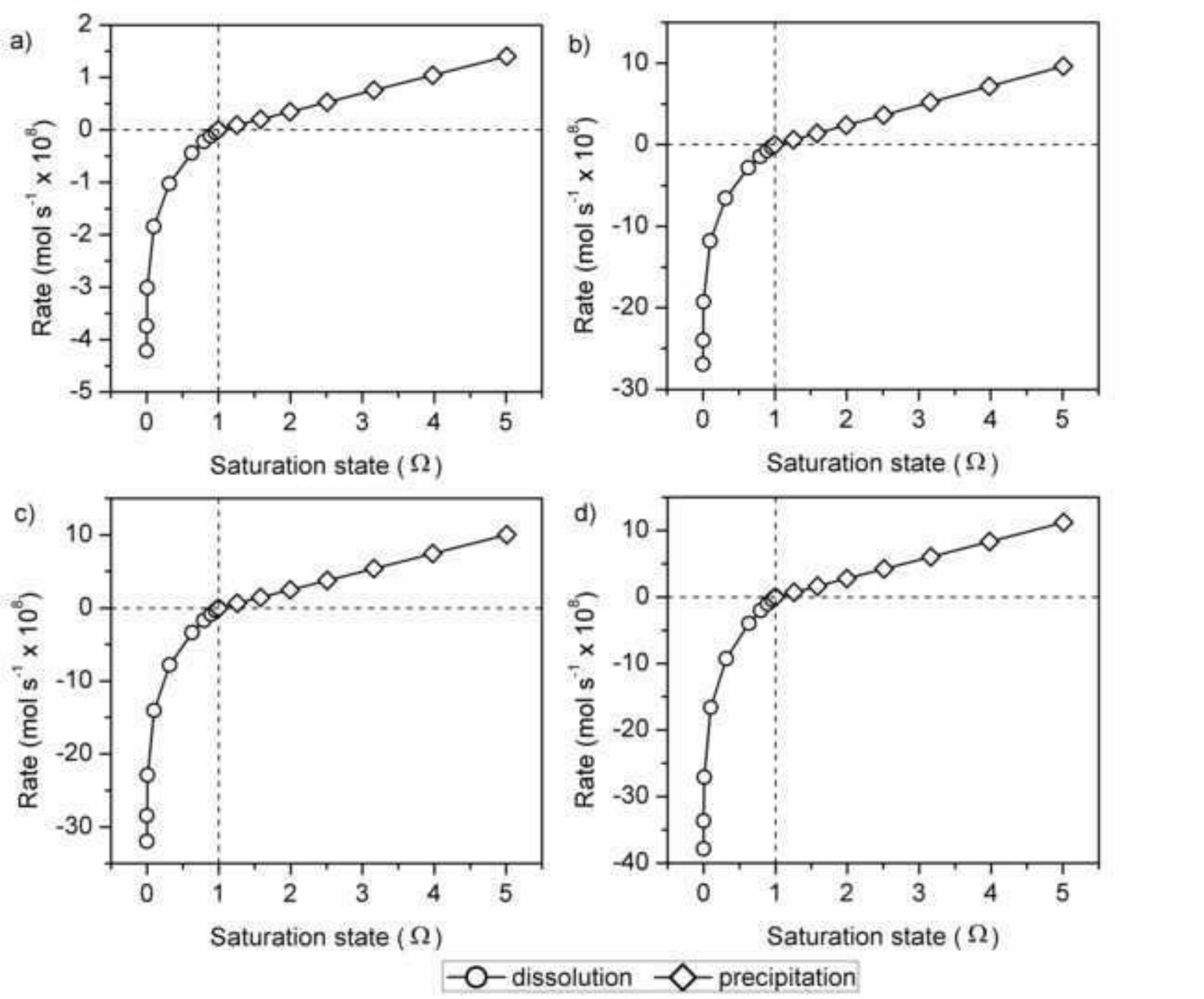

Figure A